

Theoretical and Experimental Investigation Into Machining Characteristics of VHF Micro-EDM

Qi Jing

Fudan University

Yongbin Zhang

China Academy of Engineering Physics

Lingbao Kong (✉ lkong@fudan.edu.cn)

Fudan University <https://orcid.org/0000-0003-4522-2961>

Min Xu

Fudan University

Fang Ji

China Academy of Engineering Physics

Research Article

Keywords: Micro-EDM, VHF, Surface roughness, Discharge efficiency, Material removal rate

Posted Date: May 25th, 2021

DOI: <https://doi.org/10.21203/rs.3.rs-538394/v1>

License:  This work is licensed under a Creative Commons Attribution 4.0 International License.

[Read Full License](#)

Version of Record: A version of this preprint was published at The International Journal of Advanced Manufacturing Technology on October 6th, 2021. See the published version at <https://doi.org/10.1007/s00170-021-08143-7>.

Theoretical and Experimental Investigation into Machining Characteristics of VHF micro-EDM

Qi Jing^{a,b}, Yongbin Zhang^b, Lingbao Kong^{a,*}, Min Xu^a, Fang Ji^b

^a *Shanghai Engineering Research Center of Ultra-precision Optical Manufacturing, School of Information Science and Technology, Fudan University, Shanghai, 200438, China*

^b *Institute of Machinery Manufacturing Technology, China Academy of Engineering Physics, Mianyang, 621000, China.*

* Email: LKong@fudan.edu.cn; Tel: +86-21-3124 2565

Abstract

To further explore the machining characteristics of very high-frequency micro-electrical discharge machining (VHF micro-EDM), the range of radio-frequency (RF) power amplifier was expanded to 110 MHz, and the power of the RF power amplifier was also greatly increased up to 91 W. The principle of the VHF pulse generator was discussed in detail, and an electro-thermal model suitable for VHF micro-EDM was established to determine the diameter of the plasma channel and the energy distribution ratio. Experimental studies for VHF micro-EDM were also carried out, and the effects of power and frequency on machining characteristics were then analysed and discussed. The results show that at the same frequency, the higher the power is, the higher the material removal rate (MRR) and the larger the number of discharge craters. At the same power, the MRR and the size of discharge craters both first increase and then decrease with increasing frequency and reach the maximum value at 65 MHz. For the copper workpiece, when the frequency is 110 MHz and the total power of the power amplifier is 8.0 W, 5.6% of the energy is used for the material removal of the workpiece, and the finest processing surface is obtained with the surface roughness $R_a=12$ nm. The average diameter of the discharge craters is as small as $0.268\ \mu\text{m}$, and the diameter of the plasma channel is only $0.350\ \mu\text{m}$. In addition, the effects of different workpiece materials and dielectric fluids are also analysed in this paper.

Keywords: Micro-EDM, VHF, Surface roughness, Discharge efficiency, Material removal rate.

1. Introduction

The manufacturing requirements of micro-scale parts and microstructures have become increasingly extensive with the development of modern science and technology [1]. Moreover, increasingly higher requirements of processing quality are also necessary [2]. There are many micro three-dimensional parts or microstructures that not only require higher machining

accuracy but also require no obvious micro-defects on the machined surface, a smooth surface with low roughness and higher processing efficiency. For instance, the surface quality of the slow-wave microstructures in a terahertz travelling wave tube directly determines its physical properties [3-5], and the micro-film cooling holes in the turbine blades of aeroengines have stringent requirements for machined surface integrity [6]. These factors bring more challenges to micro-machining technology.

Micro-electrical discharge machining (micro-EDM) is a non-contact machining method that removes materials by means of the extremely high temperature generated by spark discharge. There is no macro-cutting force, so it is particularly suitable for machining both hard-to-cut and easily deformed conductive materials without being affected by the mechanical properties of the materials [7]. Micro-EDM has many advantages, such as high machining accuracy, low cost and strong controllability over other micro-machining methods. Therefore, it has great development potential in the field of micro-scale three-dimensional structure machining [8].

However, micro-EDM is restricted by the demands of fine surface integrity and high processing efficiency, which are difficult to satisfy simultaneously [9-12]. Researchers have carried out many significant studies on the suppression technology of micro-surface defects in micro-EDM, which mainly focused on three aspects. The first is to suppress abnormal discharge and arcing so that good interelectrode conditions can be maintained [13, 14]. The processing efficiency is improved while the processing quality can be ensured as much as possible, but the improvement of the surface quality is limited. The second is to reduce the single discharge energy so that a smaller single erosion crater can be obtained [15]. The surface quality is finer, but there are still some problems, such as low processing efficiency and terrible debris removal conditions. The third is to employ a hybrid machining method or carry out post-processing of the machined surface with the help of other machining technologies [16-18]. The surface quality can be improved, but the processing complexity is increased and the comprehensive processing efficiency is low.

A recurring topic in micro-EDM is to obtain higher surface quality by reducing the single discharge energy. It is conducive to exploring the extreme processing ability of micro-EDM and fundamentally solving the problem of machined surface quality. The key challenge is how to reduce the single discharge energy to a lower level, while a continuous and stable machining state and high processing efficiency could also be ensured. The single discharge energy generated by the micro-EDM power supply directly affects the size of the single erosion crater and then affects the surface quality. The lower the single discharge energy is, the smaller the size of the single erosion crater. The machined surface is thereby finer [19]. Therefore, many studies have focused on the micro-EDM power supply and strived to improve the extreme processing ability of micro-EDMs.

There are three main types of traditional power supplies. For an RC-type power supply, a lower single discharge energy and finer machined surface are often obtained by reducing the voltage or the equivalent capacitance of the gap [20-22]. However, the discharge gap decreases as the voltage decreases, which easily causes frequent arcing and short circuit and then makes the machining discontinuous. In addition, the stray capacitance determines the lower limit of the

single discharge energy. For the transistor-type power supply, compressing the pulse width is a common way to reduce discharge energy [23, 24], but it is difficult to obtain micro-energy pulses with a pulse width of several nanoseconds due to hardware limitations. To further eliminate the negative influence of stray capacitance, Kunieda et al. [25] invented an electrostatic induction feeding-type power supply. The diameter of the crater eroded by this power supply was only 0.43 μm . However, the maximum frequency of this power supply is 10 MHz at present, which may limit its processing efficiency.

In addition to the traditional power supplies, A. Okada et al. [26] took the lead in applying radio frequency (RF) technology to EDM, and the pulse frequency was up to 9 MHz. They pointed out that the surface roughness was reduced due to the shorter discharge time. Hamza K. Khattaka et al. [27] explained the phenomenon of discharge between grapes in a microwave oven. Although the principle of this phenomenon is not related to micro-EDM, it produced a vision for us with micro-EDM at a higher frequency or even at a microwave frequency. Inspired by these studies, our research group developed a very high frequency (VHF, frequency range of 30 MHz~300 MHz) pulse generator based on the principle of circuit resonance in a previous study [28]. Compared with the traditional power supply, its pulse frequency is up to 90 MHz, its single discharge energy is lower, and nano-level erosion craters can be obtained. The common defects in micro-EDM, such as thermal damage, recast layers and heat-affected zones, could be greatly reduced. Moreover, the machined surface roughness was lower, and the discharge efficiency was also significantly improved due to the high frequency.

To further explore the machining characteristics and technical rules of VHF micro-EDM by using this new power supply and to master the scale range of the plasma channel in VHF micro-EDM and the distribution of energy, the VHF pulse generator is upgraded in this paper. The frequency range of the RF power amplifier is expanded to 110 MHz. The power of the RF power amplifier is also greatly increased, reaching 91 W. The principle of the VHF pulse generator is discussed in detail, and an electro-thermal model that is suitable for VHF micro-EDM is established to solve the diameter of the plasma channel and the energy distribution ratio. Finally, VHF micro-EDM experiments are carried out, and the results are discussed in detail.

2. Principle of VHF micro-EDM

VHF micro-EDM no longer follows the traditional idea, which is to compress the pulse width or reduce the voltage, current and capacitance. Instead, VHF electromagnetic oscillation is employed to realize the time modulation of the plasma channel. The plasma channel is rapidly formed and cut off alternately under the influence of VHF electromagnetic oscillation, which cannot extend completely. Moreover, according to the VHF circuit characteristics, the extremely high energy density of the plasma channel can be ensured. This method utilizes the power output of the VHF transmitting system. Schematic diagrams of the VHF transmitting system and VHF micro-EDM are shown in Fig. 1. Fig. 1(a) shows that the VHF sinusoidal signal generated by the function generator is amplified by the RF power amplifier and radiated

into the space through the antenna. A VHF micro-EDM system is established when the antenna is replaced with wires, tool electrodes and workpieces and the isolator is added, as shown in Fig. 1(b).

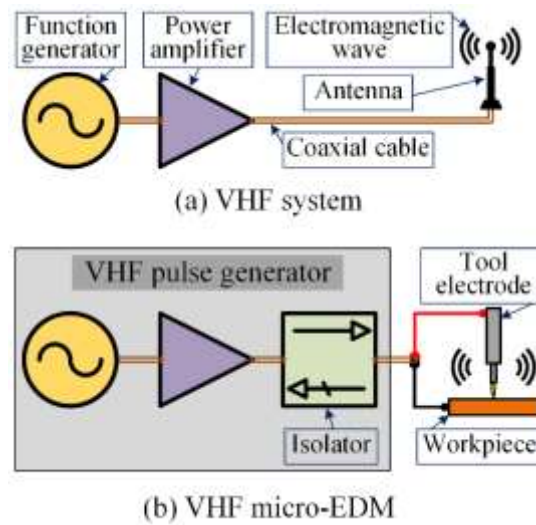


Fig. 1 Schematic diagram of the (a) VHF transmitting system and (b) VHF micro-EDM.

Because the frequency of the VHF band is high, the voltage and current may be different at different positions due to the length and attitude of the ordinary wires in VHF micro-EDM. Therefore, it is necessary to mark the position of the measurement point when measuring it. To make the measurement results closer to the true value between the tool electrode and the workpiece, it is also necessary to make the condition of the ordinary wire as similar as possible during the measurement and the processing. As shown in Fig. 2, the measuring voltage and current are shown in the picture of the oscilloscope when the signal frequency is 110 MHz and the signal amplitude is 300 mV. The voltage waveform generated by the VHF pulse generator is a bipolar sinusoidal waveform, and there is current even in the open circuit state. The current waveform is also a bipolar sinusoidal waveform, which is nearly in phase with the voltage.

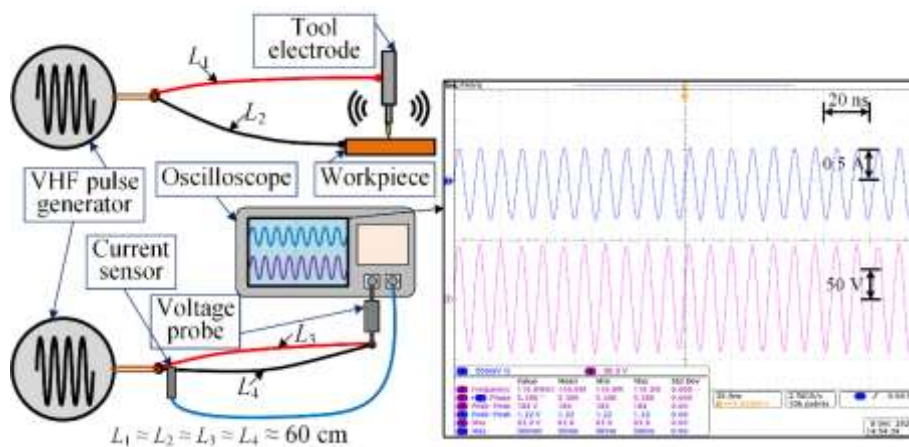


Fig. 2 Schematic diagram of the measurement and the voltage and current results.

The polarities of the tool electrode and the workpiece change according to the VHF frequency

due to the bipolar waveform of the VHF pulse generator. Hence, discharge may occur in the time range of the positive pulse or the negative pulse. The discharge principle is shown in Fig. 3. The workpiece acts as the negative electrode when the positive pulse discharges, and is mainly bombarded by the positive ions. Similarly, the workpiece acts as the positive electrode when the negative pulse discharges, and is mainly bombarded by electrons.

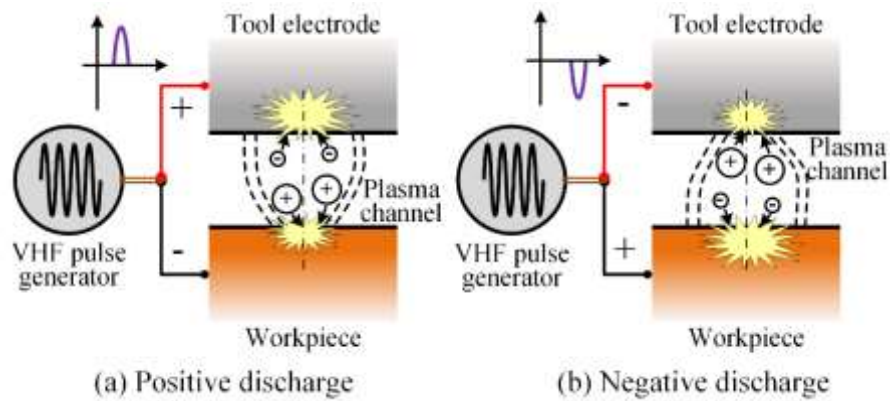


Fig. 3 Discharge principle of the VHF pulse generator: (a) positive discharge and (b) negative discharge.

For traditional power supplies, on the one hand, the single discharge energy can be calculated according to the voltage and current data collected during discharge because the frequency is relatively low. On the other hand, the single discharge energy can also be estimated according to pre-set parameters such as the pulse width, peak voltage and current-limiting resistance. However, for the VHF pulse generator, the voltage and current data during discharge may contain more information, and the data are not always accurate for the measurement of the single discharge energy. Furthermore, the VHF pulse generator has different responses as the load changes. Fig. 4 shows the whole equivalent circuit of VHF micro-EDM, where R_0 , L_0 , C_0 , G_0 and dx are parameters related to the transmission line. R_L and L_L represent the equivalent resistance and inductance of ordinary wires. $R_g(t)$, $L_g(t)$ and $C_g(t)$ represent the resistance, inductance and capacitance characteristics, respectively, of the discharge gap. C_S is the stray capacitance existing in the discharge gap. Obviously, the impedance of the discharge gap changes according to the three common discharge states of the micro-EDM, which are the open circuit discharge spark and short circuit. For the VHF pulse generator, the energy distribution is affected since the load changes. In addition, the changes in impedance are frequency-dependent due to the existence of capacitive reactance and inductive reactance. Therefore, the adjustment of the frequency of the VHF pulse generator also leads to a difference in the load response and then has an influence on the discharge energy.

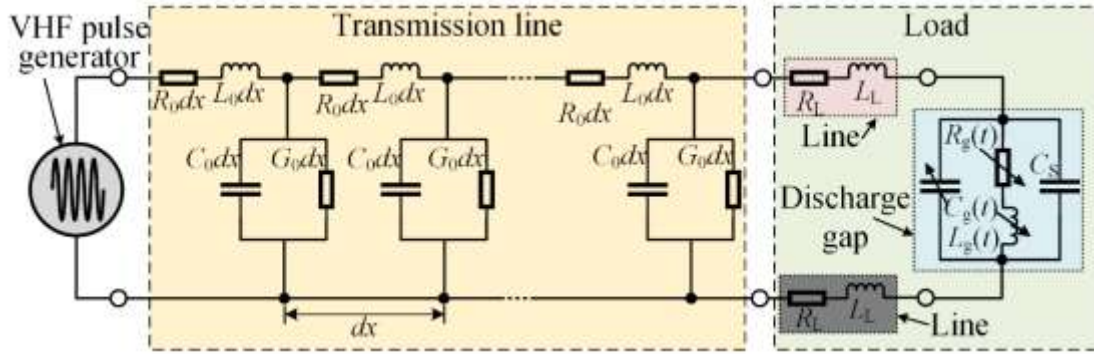


Fig. 4 The whole equivalent circuit of VHF micro-EDM.

3. Electro-thermal model of VHF micro-EDM

To study the erosion characteristics of VHF micro-EDM, it is very important to accurately obtain the single discharge energy, the fraction of the energy distributed to the workpiece and the diameter of the plasma channel generated by the discharge. However, it is difficult to obtain the single discharge energy directly by measurement at present because the principle of the VHF pulse generator is very different. Some scholars [29, 30] measured the size of the craters generated by single-pulse experiments and established electro-thermal models for micro-EDM. Then, the fraction of the energy distribution and the diameter of the discharge plasma channel could be calculated through a reverse solution method, but this was based on the accurate measurement of the voltage and current data and the accurate calculation of the single discharge energy.

For the VHF micro-EDM, the total power of the system can be accurately obtained by the RF power metre. Since its essence is to vaporize and melt the workpiece material although the high temperature generated by discharge, the existing micro-EDM heat source theory and model [31-34] and the reverse solution method can be employed for studying the energy distribution and the diameter of the plasma channel in VHF micro-EDM. To simplify the model, the following reasonable assumptions are devised.

Assumptions:

- (1) Since the pulse frequency has reached the VHF band, the pulse width is less than 15 ns. The positive ions can hardly reach the negative electrode in such a short time according to previous micro-EDM studies [35, 36], so there is almost no material removal of the negative electrode. Therefore, the negative electrode is not appreciably eroded during VHF micro-EDM. Therefore, it is assumed that the erosion craters on the workpiece are all generated when the workpiece is the positive electrode. The diameter of the crater on the workpiece can be obtained by measuring and averaging several complete discharge craters on the surface of the workpiece because it is difficult to carry out a single-pulse discharge experiment for the VHF pulse generator.
- (2) Similarly, the depth of the crater on the workpiece also needs to be obtained through assumptions and calculations without the single-pulse discharge experiment. There are

many assumptions about the depth in previous studies [37-39]. Generally, a single erosion crater is simplified as a spherical crown, as shown in Fig. 5(a), where z_m is the depth of the crater and d_m and r_m are the diameter and radius of the crater, respectively. It is considered that the discharge crater is generally smaller than the hemispherical shape, so $z_m < r_m$. Ideally, the craters do not overlap at all, as shown in Fig. 5(b), where l is the distance between the centres of the two adjacent craters, and Ra represents the surface roughness, so $z_m = 4Ra$ according to the definition of Ra . The craters must overlap partially, as shown in Fig. 5(c), so $z_m > 4Ra$. Therefore, $4Ra < z_m < r_m$, and the depth of the crater is calculated as Eq. (1) to minimize the error as much as possible.

$$z_m = \frac{r_m + 4Ra}{2} \quad (1)$$

- (3) Assuming that the plasma channel is axisymmetric, a two-dimensional axisymmetric model is used to simplify the calculation.
- (4) The heat transfer to the workpiece is only by heat conduction, and the radiation and convection are negligible.
- (5) The heat flux on the workpiece due to discharge is Gaussian heat flux [34]. The simulation model is shown in Fig. 6. The research object is the situation when the workpiece is the positive electrode, so the power source of the Gaussian heat flux reaches the positive electrode. The workpiece geometric model is large enough, with a length of 20 μm and a width of 10 μm to ensure the accuracy of the simulation.
- (6) The discharge process is assumed to be affected by the instantaneous power, as shown in Fig. 2, where the voltage and current are both sinusoidal and in phase. Therefore, the change in instantaneous power can be derived from the average power, as shown in Eq. (12).
- (7) The changes in the diameter of the plasma channel and the fraction of energy distribution over time during the discharge process are ignored. These two quantities are taken as constants.
- (8) The superheated area, whose temperature is above the boiling point, is removed from the workpiece, and the others are not removed.

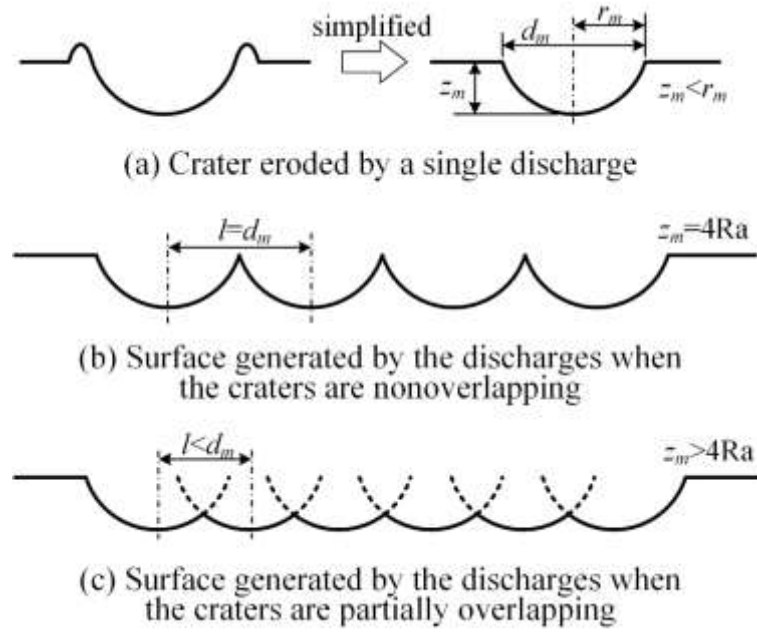


Fig. 5 Simplification of the crater: (a) crater eroded by a single discharge, (b) surface generated by the discharges when the craters are nonoverlapping and (c) surface generated by the discharges when the craters are partially overlapping.

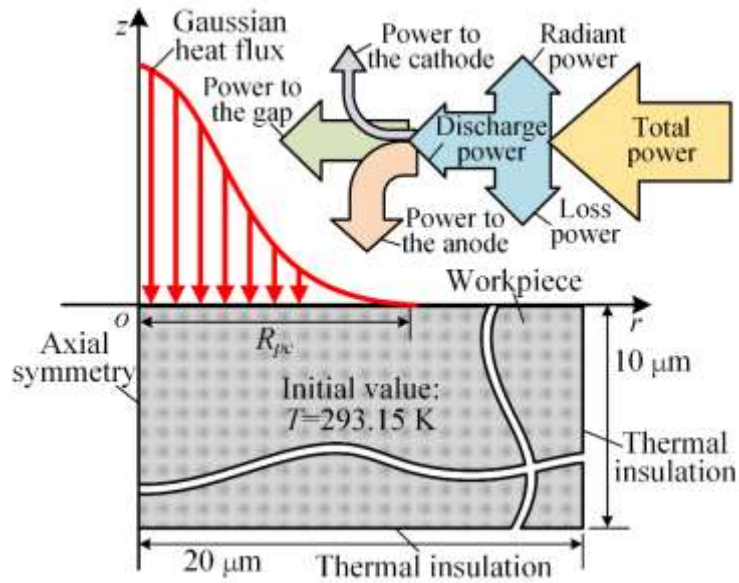


Fig. 6 Schematic diagram of simulation model.

Based on the above assumptions, the electro-thermal model of VHF micro-EDM can be constructed as follows. The energy source of the entire VHF micro-EDM system is completely provided by the RF power amplifier. The total average power can be measured by the power metre; then, Eq. (2) can be obtained according to the conservation of energy.

$$P_T = P_L + P_R + P_D \quad (2)$$

where P_T is the total average power output by the power amplifier. P_L is the sum of all the average power losses, which mainly includes feeder loss and return loss. P_R is the average RF radiation power. P_D is the total average power used for discharge. Therefore, a coefficient can be defined as shown in Eq. (3).

$$\eta = \frac{P_D}{P_T} \quad (3)$$

where η represents the efficiency of the VHF pulse generator. Only a part of the total discharge power is used for the material removal of the workpiece, so a coefficient can be defined as shown in Eq. (4).

$$\lambda = \frac{P_{AVG}}{P_D} \quad (4)$$

where λ is the common energy distribution coefficient in micro-EDM, which represents the energy ratio transferred to the workpiece. Thus, P_{AVG} is the average power for the material removal of the workpiece. It can also be expressed as follows:

$$P_{AVG} = \lambda \eta P_T = \phi P_T \quad (5)$$

where ϕ is the fraction of the energy distributed to the workpiece relative to the total power output by the power amplifier in this paper. The governing partial differential equation of Fourier heat transfer is Eq. (6).

$$\frac{1}{\alpha} \frac{\partial T}{\partial t} = \frac{\partial^2 T}{\partial r^2} + \frac{1}{r} \frac{\partial T}{\partial r} + \frac{\partial^2 T}{\partial z^2} \quad (6)$$

where T is the temperature distribution function, t is the time, r is the radial distance, z is the axial distance and α is the thermal diffusivity of the material, which can be expressed as

$$\alpha = \frac{K_t}{\rho C_p} \quad (7)$$

where K_t is the average thermal conductivity of the material, ρ is the density of the material and C_p is the specific heat of the material. The Eq. (8) [40] is used to express the equivalent specific heat C_{PE} in the simulation model, where the latent heat is coupled to the specific heat of the material, considering the phase transition of the material.

$$C_{PE} = C_p + \delta_m L_m + \frac{L_m}{T_m} \cdot H'((T - T_m), \Delta T) + \delta_v L_v + \frac{L_v}{T_v} \cdot H'((T - T_v), \Delta T) \quad (8)$$

$$\delta_m = \frac{\exp[-(T - T_m)^2 / \Delta T^2]}{\Delta T \sqrt{\pi}} \quad \delta_v = \frac{\exp[-(T - T_v)^2 / \Delta T^2]}{\Delta T \sqrt{\pi}}$$

where H' is the smooth Heaviside function, δ_m and δ_v are the regular functions (K^{-1}) near the melting and boiling points, respectively, and ΔT is the half-width of the curve, which determines the width of the smooth Heaviside function and the regular function. ΔT can be selected according to the requirement. The smaller the value, the closer to the real situation. L_m and L_v are the latent heat of melting and vaporization, respectively. Therefore, the modified thermal diffusivity α' can be expressed as follows:

$$\alpha' = \frac{K_t}{\rho C_{PE}} \quad (9)$$

The Gaussian heat flux is given by:

$$q(r) = q_0 \exp\left[-4.5 \left(\frac{r}{R_{pc}}\right)^2\right] \quad (10)$$

where R_{pc} is the diameter of the plasma channel and q_0 is given by:

$$q_0 = \frac{4.57 P_{AVG}}{\pi R_{pc}^2} = \frac{4.57 \varphi P_T}{\pi R_{pc}^2} \quad (11)$$

According to assumption (6), the instantaneous power $P_{INS}(t)$ is expressed as

$$P_{INS}(t) = P_{PEAK} \frac{1 - \cos(4\pi ft)}{2} = P_{AVG} [1 - \cos(4\pi ft)] \quad (12)$$

where P_{PEAK} is the peak power for the material removal of the workpiece and f is the frequency. Thus, the Gaussian heat flux is finally given by

$$q(r, t) = q_0(t) \exp \left[-4.5 \left(\frac{r}{R_{pc}} \right)^2 \right] \quad (13)$$

where $q_0(t)$ is

$$q_0(t) = \frac{4.57 P_{INS}(t)}{\pi R_{pc}^2} = \frac{4.57 \varphi P_T [1 - \cos(4\pi ft)]}{\pi R_{pc}^2} \quad (14)$$

The initial condition of the model is

$$T(r, z, 0) = T_0 \quad (15)$$

where T_0 is the initial temperature of the workpiece material and is also the ambient temperature of 293.15 K. The boundary conditions are

$$-K_t \frac{\partial T(r, 0, t)}{\partial z} = \begin{cases} q & 0 < r < R_{pc} \\ 0 & r > R_{pc} \end{cases} \quad (16)$$

$$T(\infty, \infty, t) = T_0 \quad (17)$$

The model was solved in the COMSOL Multiphysics software. The physical property parameters of the material are listed in Table 1, and the solution procedure is shown in Fig. 7. First, the radius and depth of the crater were measured and calculated. Second, the fraction of the energy distribution φ and the radius of the plasma channel R_{pc} are presupposed. Then, the heat conduction model was solved, so the radius and depth of the crater according to the vaporization area can be calculated. Finally, the measured and calculated results were compared. If the difference was less than the set error limit (5 nm), it was considered that φ and R_{pc} were confirmed. Otherwise, new φ and R_{pc} were presupposed, and the process was repeated. The calculation results are shown in Fig. 8 when the output voltage amplitude of the function generator is 100 mV, and the frequency is 65 MHz and 110 MHz. The time points for material removal are less than those of the pulse width due to the instantaneous power, which are 5.5385 ns and 2.4545 ns, respectively. φ and R_{pc} are 27.58% and 0.417 μm , respectively, when the frequency is 65 MHz, and φ and R_{pc} are 5.6% and 0.175 μm , respectively, when the frequency is 110 MHz.

Table 1 Physical properties of copper.

Physical Properties (293.15 K)	Copper
Specific heat [J/(kg·K)]	386
Latent heat of melting [J/kg]	2.05e5
Latent heat of vaporization [J/kg]	4.8e6
Density [kg/m ³]	8960
Melting point [K]	1356.55
Boiling point [K]	2833.15
Thermal conductivity [W/(m·K)]	397

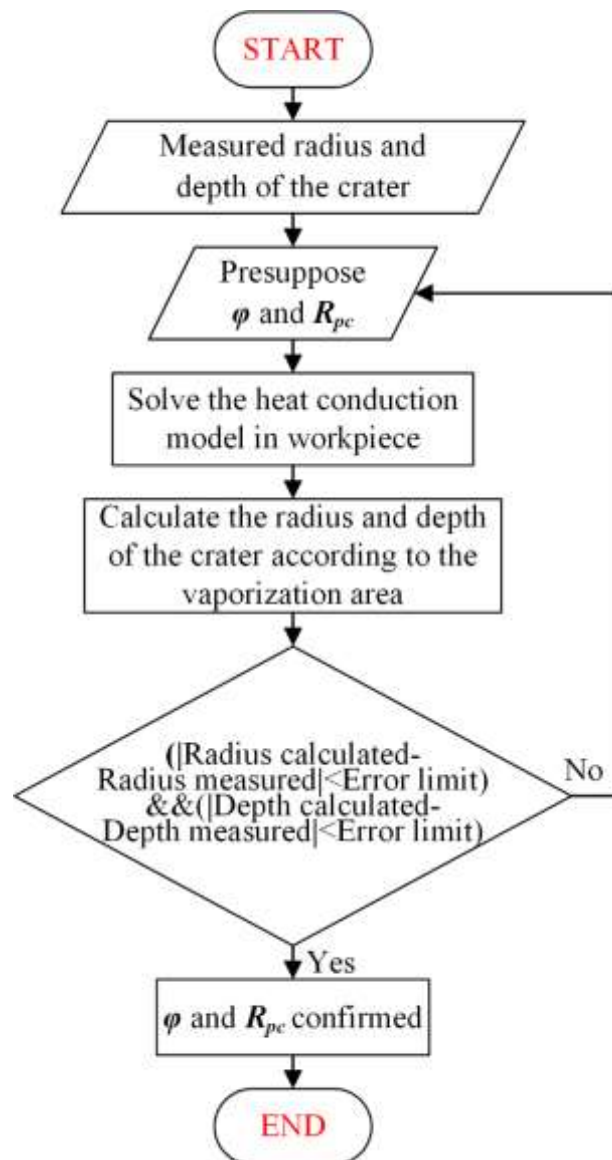


Fig. 7 Flowchart of the solution procedure.

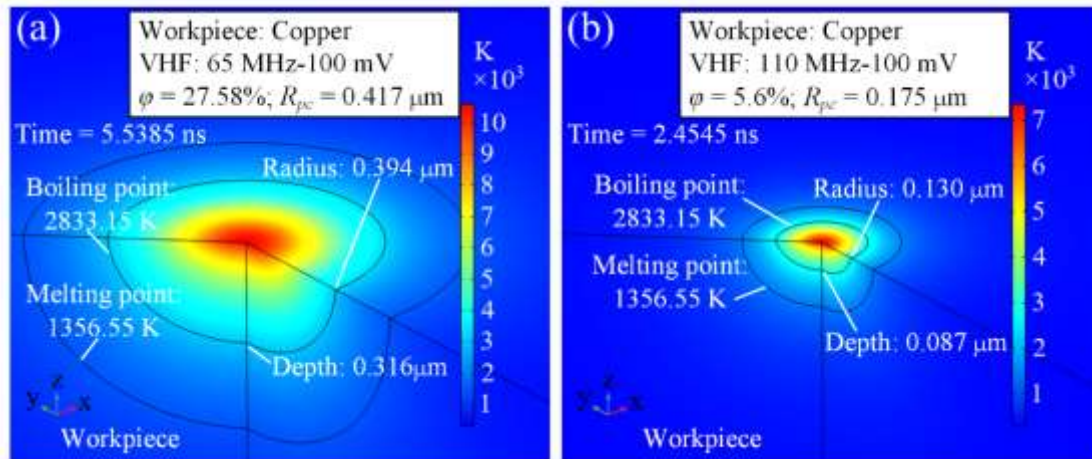


Fig. 8 Calculation results of (a) 65 MHz-100 mV and (b) 110 MHz-100 mV.

4. Experimental design

The VHF micro-EDM discharge erosion experiment was performed on a three-axis experimental platform. The tool electrode was clamped on the Z axis. The workpiece was fixed on the X-Y platform and immersed in the dielectric fluid. The tool electrode was slowly fed closer to the workpiece for discharging. Microscopic imaging equipment was employed to observe the discharge state between the tool electrode and the workpiece so that a continuous and stable discharge process could be achieved. The processing time was also recorded. The experimental materials of the tool electrode, workpiece and dielectric fluid are listed in Table 2. The power output of the power amplifier was adjusted by adjusting the voltage amplitude of the function generator in the experiment. The relation between the amplitude of the signal source and the total power output of the VHF pulse generator is shown in Fig. 9. The parameters of the VHF pulse generator are listed in Table 3. The check mark means that the experiment can be carried out successfully with the parameter combination, and the cross means that the continuous discharge experiment is difficult to carry out without automatic monitoring and servo control because the energy is too high.

All the tool electrodes and workpiece after discharge erosion experiments were ultra-sonically cleaned before the measurement. For the experiments that were to determine the material removal rate (MRR) and tool electrode wear ratio (TWR), the processing time was relatively long to ensure the accuracy of the measurement results. Then, the tip diameter of the tool electrode after processing was observed using an optical microscope (Nikon) to calculate the wear volume based on the geometric relationship. The volume of the material removal areas was measured using a digital microscope (VHX-6000, Keyence). The average value of multiple measurements was used to calculate the MRR by combining the corresponding processing time. In addition, for the experiments that measured the diameter of the crater and the surface roughness, the processing time was relatively short to just ensure a complete erosion area on the surface of the workpiece. Then, the erosion area on the workpiece was observed using a scanning electron microscope (SEM, Zeiss). Several complete single discharge craters were

selected to measure the diameter, and the average value was the measured diameter. The surface roughness Ra of the erosion area on the workpiece was measured by a white light interferometer (WLI, Sensofar), and the average value was obtained by multiple measurements.

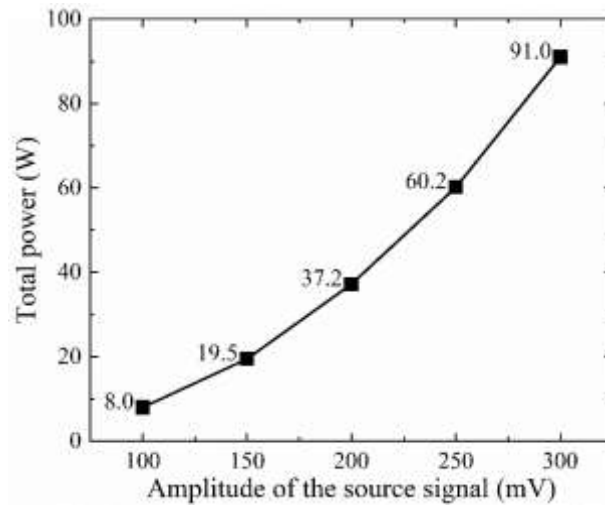


Fig. 9 Relation between the total power and the amplitude of the source signal.

Table 2 Experimental materials.

Tool electrode	Conical stainless-steel electrode with a tip diameter of 125 μm
Workpiece	Copper, Brass, Stainless steel, Aluminium, Ni-base superalloy
Dielectric fluid	EDM oil, Ultrapure water

Table 3 Parameters of the VHF pulse generator.

Frequency [MHz]	Voltage amplitude of the function generator [mV]				
	100	150	200	250	300
55	√	√	√	×	×
60	√	√	×	×	×
65	√	√	×	×	×
70	√	√	×	×	×
90	√	√	√	√	√
100	√	√	√	√	√
110	√	√	√	√	√

5. Results and discussions

5.1 Observation of the phenomenon in the processing

Some significant discharge states under different processing conditions were recorded by microscopic imaging equipment. Pictures of the copper workpiece eroded in the EDM oil are

shown in Fig. 10. Fig. 10(c) shows the discharge conditions when the voltage amplitude of the signal source was 100 mV and the frequency range was 55 MHz-70 MHz. Continuous and stable blue-white sparks and a large number of bubbles were generated during processing. When the frequency was 90 MHz, as shown in Fig. 10(d), there were continuous and stable but relatively weak orange-white sparks and still many bubbles but relatively few bubbles during processing. When the frequency was 110 MHz, the discharge was weaker than that at 90 MHz, and a weak arcing phenomenon occurred occasionally, as shown in Fig. 10(e). When the frequency was 65 MHz and the voltage amplitude of the signal source was 150 mV, as shown in Fig. 10(b), there were raging blue-white sparks accompanied by a large number of bubbles. When the voltage amplitude of the signal source was up to 200 mV, the raging orange-white arc almost flooded the whole processing area, as shown in Fig. 10(a). The tool electrode and the workpiece were scorched, and the processing was difficult to continue due to the lack of automatic monitoring and servo control.

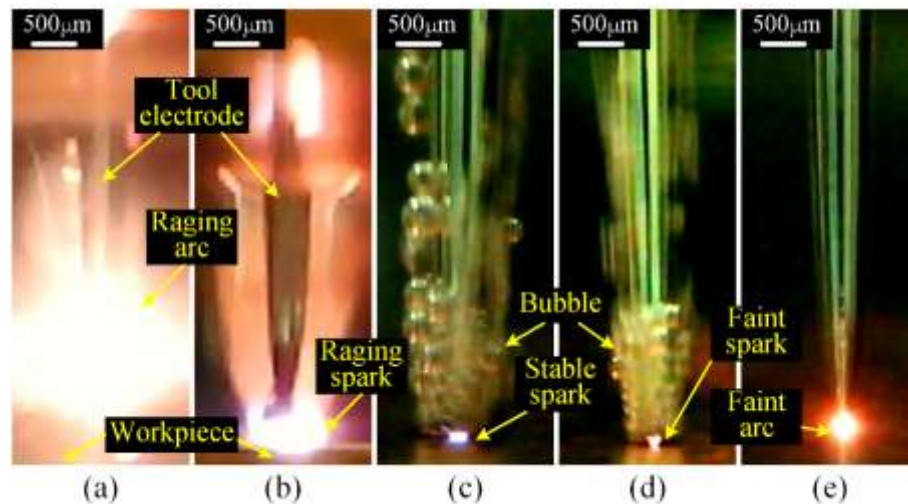


Fig. 10 Pictures of the processing in EDM oil under different conditions: (a) 65 MHz-200 mV, (b) 65 MHz-150 mV, (c) 65 MHz-100 mV, (d) 90 MHz-100 mV and (e) 110 MHz-100 mV.

Fig. 11(a) and (b) show the discharge states of the brass workpiece eroding under the condition of 60 MHz-150 mV in EDM oil and ultrapure water, respectively. There were continuous and stable blue-white sparks in both. However, the obvious difference is that a large number of bubbles appeared and escaped quickly to the liquid level when the dielectric fluid was EDM oil, and only a few bubbles gathered around the erosion area when the dielectric fluid was ultrapure water. The reason is that the EDM oil was cracked to produce gas at the high temperature generated by the discharge, while there was no gas produced by cracking in the ultrapure water, and only a few gases may be produced due to weak electrolysis.

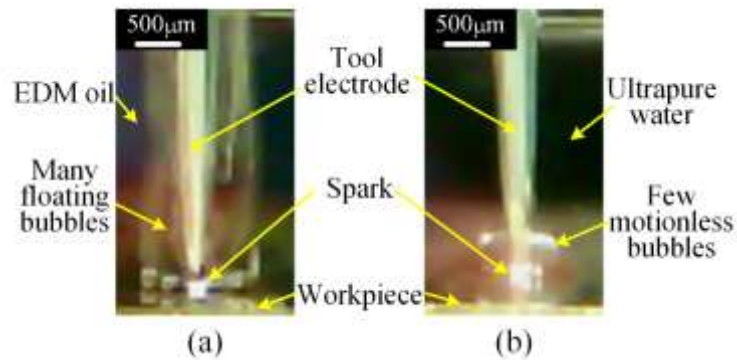


Fig. 11 Pictures of the processing under 60 MHz-150 mV in (a) EDM oil and (b) ultrapure water.

5.2 Effects of frequency and power

A series of discharge erosion experiments on the copper workpiece were carried out according to the available parameters in Table 3. The WLI and SEM measurement results of some typical machining results are shown in Fig. 12. It can be seen from Fig. 12 (a), (b) that when the total power output of the power amplifier was the same, the discharge craters of 65 MHz were larger and the surface roughness Ra was also larger, while the erosion surface of 110 MHz was very fine. The erosion surface of 110 MHz shows no obvious difference from the surrounding non-erosion polished area, and its roughness Ra was only 12 nm, which showed that the single discharge craters were at a very small level. When the frequency is 110 MHz, by comparing Fig. 12(b)-(f), the diameter of the crater and the roughness Ra increase gradually as the total power increases.

The variation curves of all the processing results with the variation of voltage amplitude of source signal and frequency are plotted as shown in Fig. 13, which are MRR, the diameter of crater, surface roughness Ra and TWR. It can be seen from Fig. 13(a), (c) and (e) that all the results increase with the voltage amplitude of the source signal for a certain frequency. Fig. 13(b), (d) and (f) show that these results first increase and then decrease with increasing frequency and reach the maximum value at 65 MHz. As analysed in Section 2, the VHF micro-EDM system has different responses to frequency, which can be understood as a state of resonance. This means that 65 MHz is the resonance point under the experimental conditions in this paper, so the energy for discharge is higher under the same total power conditions. The TWR does not show a clear trend as above with the voltage amplitude and frequency, as shown in Fig. 13(g), (h). However, the TWRs are basically approximately 160%. The reason is that the VHF pulse generator is a bipolar power supply, as analysed in Section 2. The positive and negative electrodes are continuously alternating, so the times for them to act as positive or negative electrodes are equal. Therefore, there is no obvious polarity effect in VHF micro-EDM, and the TWR is mainly related to the physical properties of the two materials. The TWR is greater than 100%, which indicates that the material is easier to remove from stainless steel than from copper.

The diameter of the plasma channel and the fraction of the energy distribution φ under each

experimental condition were calculated according to the model in Section 3, as shown in Fig. 14. Fig. 14 (a) shows that ϕ decreases with increasing voltage amplitude of the source signal for a certain frequency. Fig. 14 (b) and (d) show that ϕ and the diameter of the plasma channel first increase and then decrease with increasing frequency and reach their maximum values at 65 MHz. This also demonstrates that there is a resonant state at 65 MHz so that a larger proportion of energy is used in the micro-EDM. Moreover, the plasma channel expands more rapidly because of the higher energy. Fig. 14 (c) shows that when the frequency is 90 MHz or less, the diameter of the plasma channel increases with the voltage amplitude of the signal source. When the frequency is greater than 90 MHz, the diameter of the plasma channel first increases and then decreases with increasing voltage amplitude of the signal source. The probable reason may be that the plasma channel becomes unstable when the frequency and power are sufficiently large. Its true expansion time may be shorter, so the final diameter of the plasma channel is smaller. The energy density of the plasma channel is very high in this case. Therefore, it can be inferred that a larger depth-to-diameter ratio of discharge craters can be obtained if the power and frequency are higher in VHF micro-EDM.

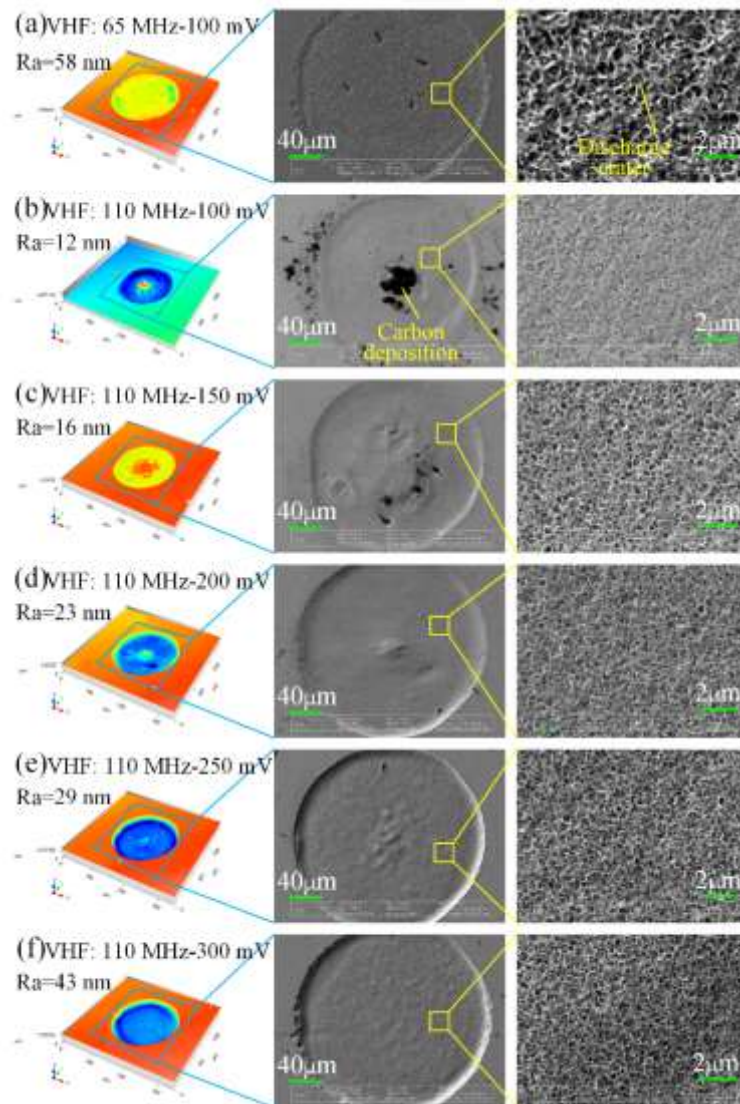
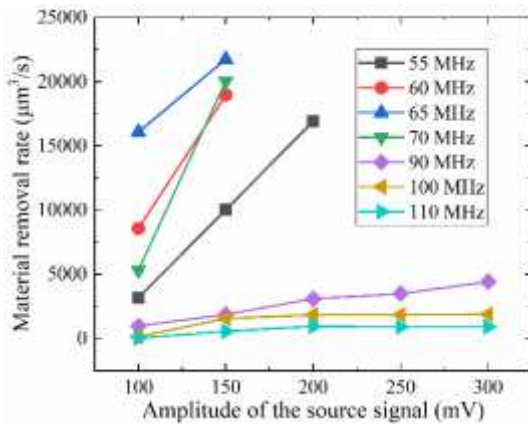
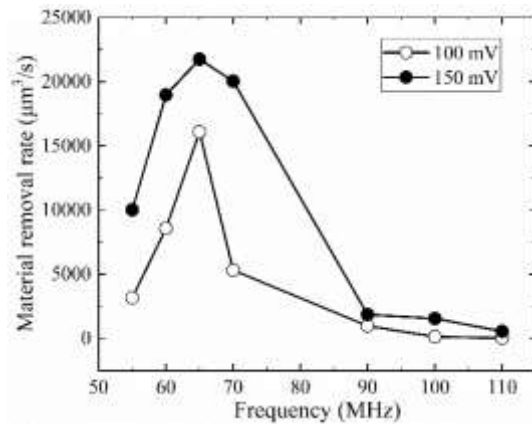


Fig. 12 WLI and SEM images of the copper workpiece under (a) 65 MHz-100 mV, (b) 110

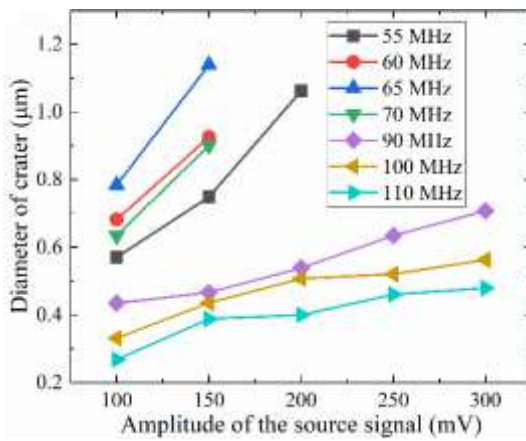
MHz-100 mV, (c) 110 MHz-150 mV, (d) 110 MHz-200 mV, (e) 110 MHz-250 mV and (f) 110 MHz-300 mV.



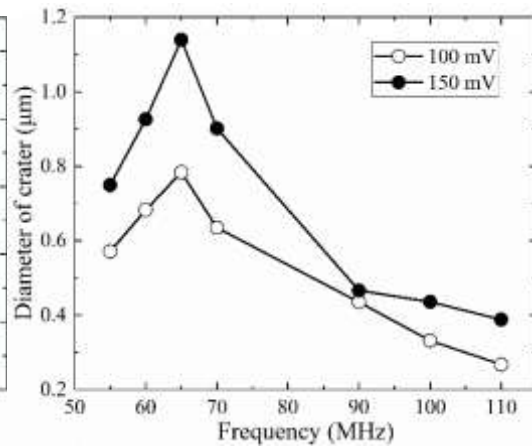
(a)



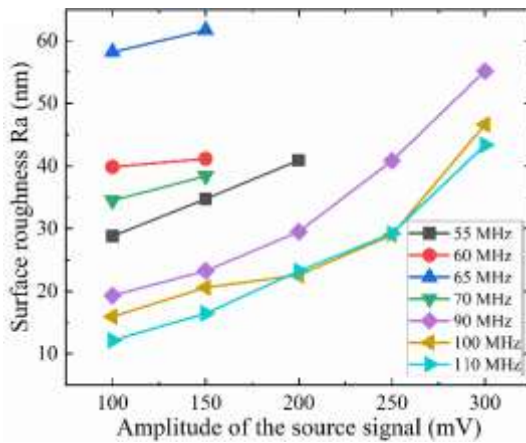
(b)



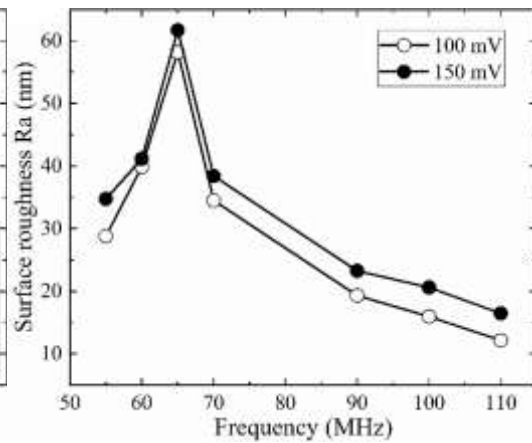
(c)



(d)



(e)



(f)

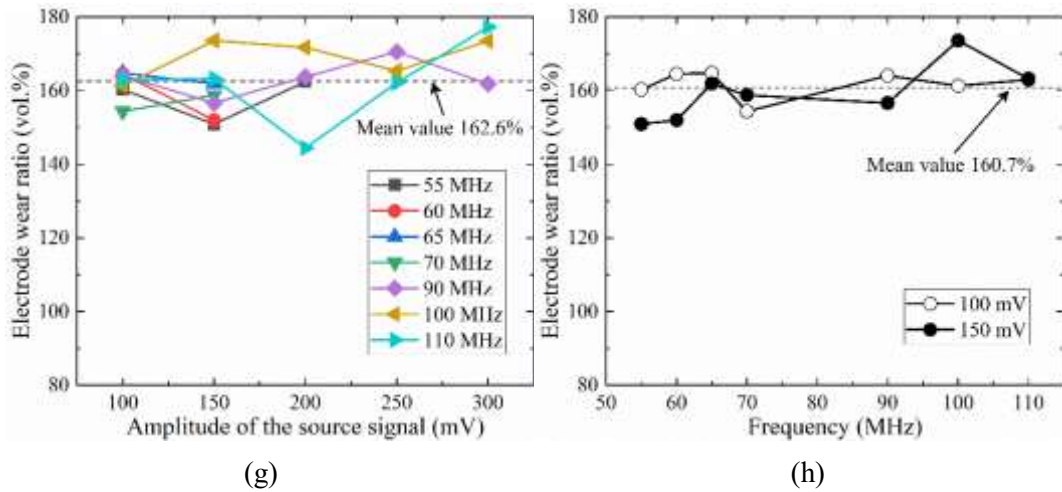


Fig. 13 Variation curves of all the processing results with the variation of voltage amplitude of the source signal and frequency: variations of (a) MRR with amplitude, (b) MRR with frequency, (c) diameter of crater with amplitude, (d) diameter of crater with frequency, (e) Ra with amplitude, (f) Ra with frequency, (g) TWR with amplitude and (h) TWR with frequency.

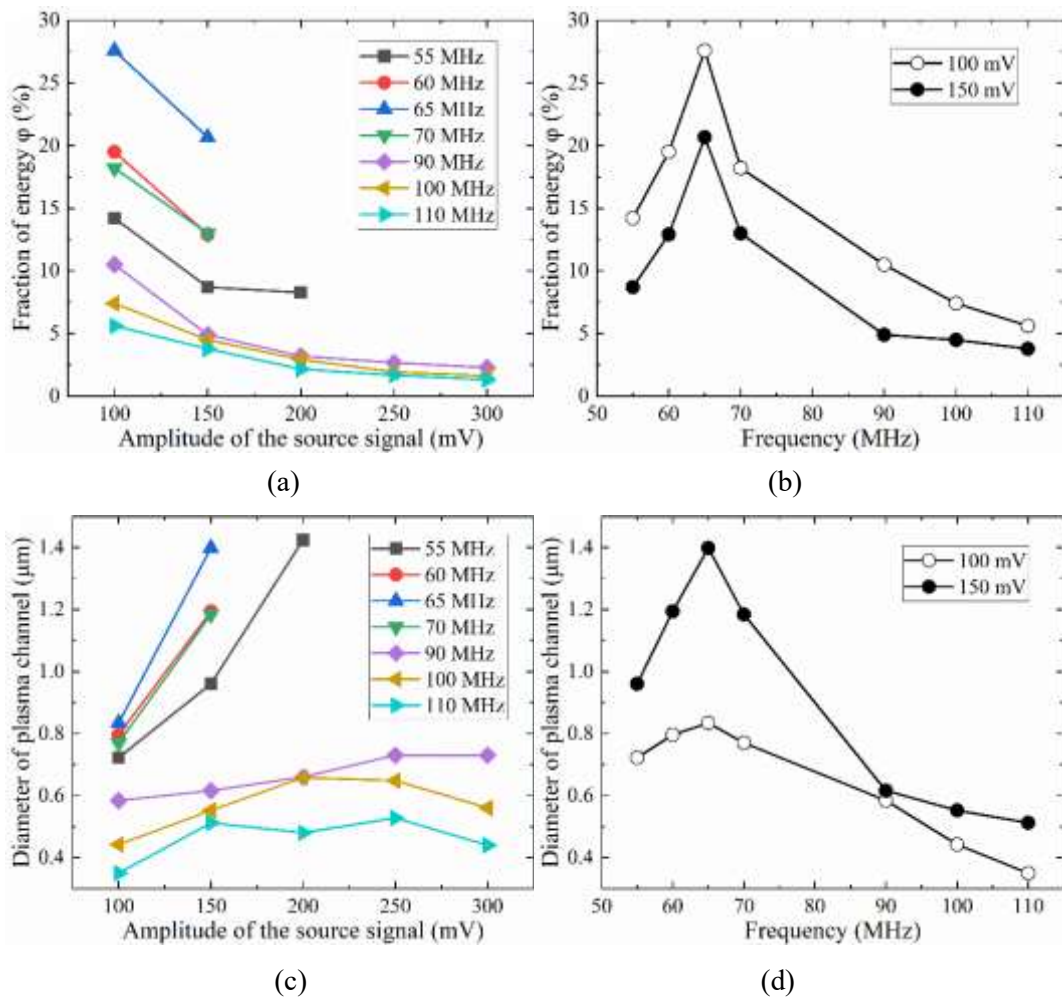


Fig. 14 Variation curves of the calculation results with the variation of voltage amplitude of the source signal and frequency: variations of (a) φ with amplitude, (b) φ with frequency, (c) diameter of plasma channel with amplitude and (d) diameter of plasma channel with

frequency.

5.3 Effects of the materials of the workpiece

Discharge erosion experiments on different workpiece materials were carried out under two parameters: 60 MHz-150 mV and 90 MHz-150 mV. The energy of 90 MHz-150 mV is too low to break down the surface oxide layer of aluminium or to remove material from the Ni-base superalloy, so the corresponding experimental data are invalid.

The processing results of MRR and TWR of different workpiece materials are shown in Fig. 15. Therefore, the MRRs of brass and aluminium are both higher because of their lower melting point, but the MRR of brass is higher due to its lower thermal conductivity. In contrast, the MRR of copper is lower because it has the best thermal conductivity. Ni-base superalloys are hard-to-machine materials due to their excellent high-temperature properties, so their MRR is the lowest. As analysed above, the TWR is mainly related to the physical properties of the two materials. The TWR is close to 100% when the workpiece material is stainless steel because the tool electrode is also stainless steel. Therefore, the TWR of other materials also reflects the processing difficulty compared to stainless steel. A TWR higher than 100% indicates that it is more difficult to process than stainless steel, and a TWR less than 100% indicates that it is easier to process than stainless steel. It is proven that the erosion mechanism of VHF micro-EDM is consistent with traditional micro-EDM theory, and the thermal physical properties of the material determine the difficulty of discharge erosion. Combined with the analysis in Section 5.2, different discharge energies can be achieved by adjusting the frequency and power in VHF micro-EDM to meet different processing requirements.

The WLI and SEM measurement results of the machining results of copper, brass and stainless steel are shown in Fig. 16 and Fig. 17. Fig. 16 shows that the discharge craters of the three materials under 60 MHz-150 mV are all larger, and the Ra values are all approximately 40 nm. Fig. 17 shows that the processed surfaces of the three materials under 90 MHz-150 mV are very fine and smooth, and the Ra values are all less than 30 nm. The comparison of the crater diameter and surface roughness of the three materials is shown in Fig. 18. The roughness of brass is the largest, which is consistent with the MRR, but the diameter of the crater of the stainless steel is the largest.

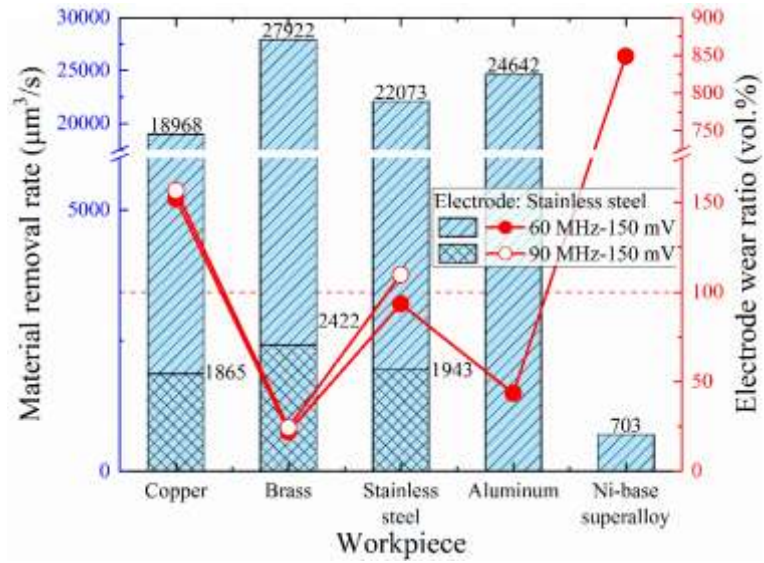


Fig. 15 MRR and TWR with different workpiece materials.

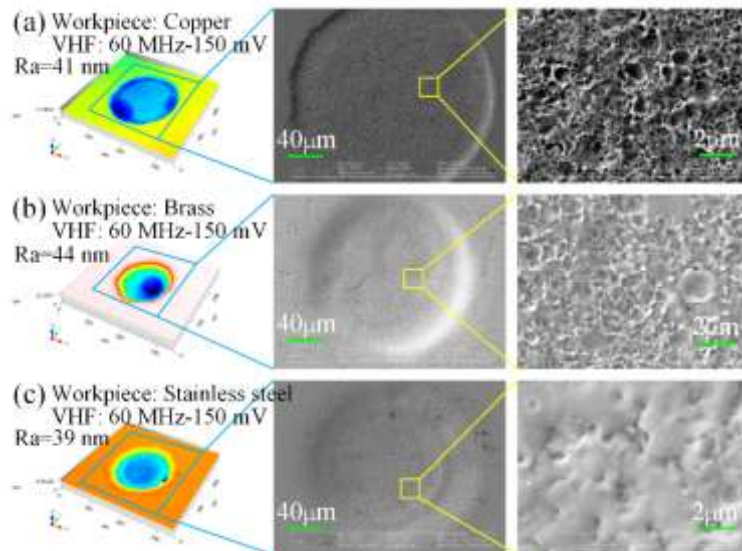


Fig. 16 WLI and SEM images of different workpieces under 60 MHz-150 mV: (a) copper, (b) brass and (c) stainless steel.

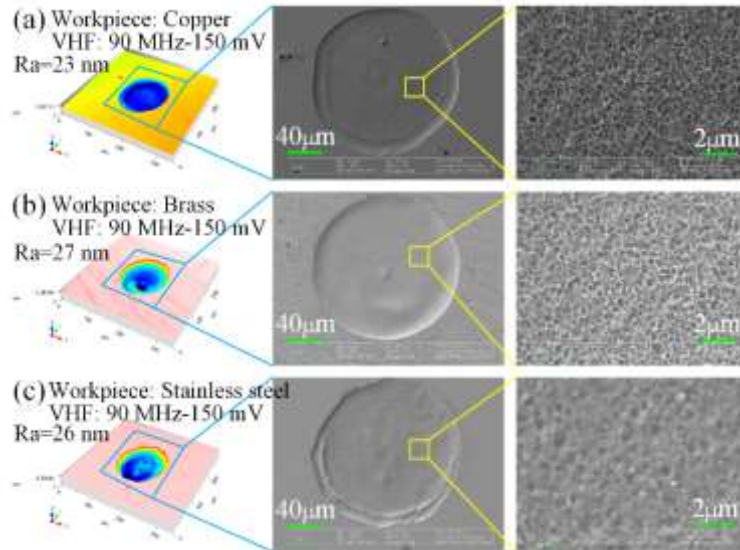


Fig. 17 WLI and SEM images of different workpieces under 90 MHz-150 mV: (a) copper, (b) brass and (c) stainless steel.

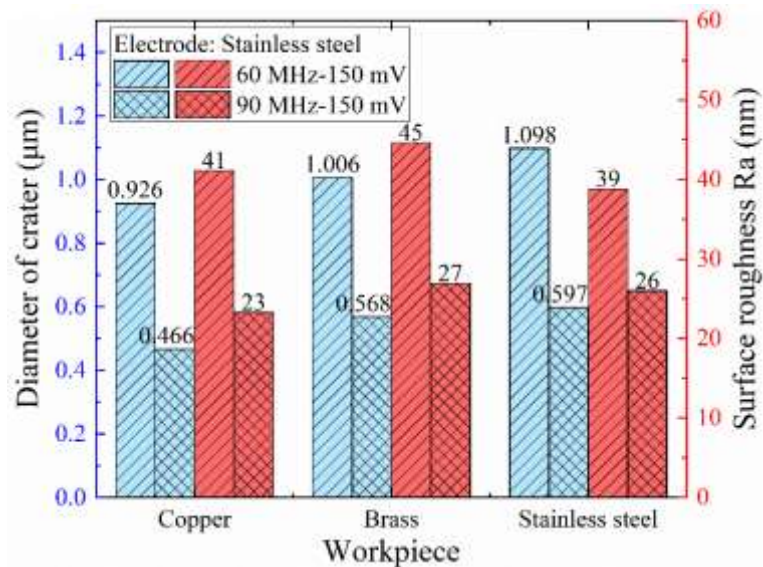


Fig. 18 Diameter of crater and Ra with different workpiece materials.

5.4 Effects of dielectric fluid

Currently, deionized or ultrapure water is also a common working fluid in many cases according to different processing requirements in the field of micro-EDM [41, 42]. To explore the erosion characteristics of VHF micro-EDM in ultrapure water, discharge erosion experiments of copper and brass in ultrapure water were carried out under 60 MHz-150 mV. The results of MRR are shown in Fig. 19. The MRR in ultrapure water is much lower than that in EDM oil whether it is copper or brass. On the one hand, according to the analysis in Section 2, although the insulation performance of ultrapure water is lower than that of EDM oil, the discharge energy may be different due to different loads of the VHF pulse generator, which makes the discharge energy in ultrapure water lower. On the other hand, as shown in Fig. 11, a large number of

bubbles generated by the cracking of EDM oil can take away the products quickly, which is conducive to the stable discharge process. However, there are almost no obvious bubbles in ultrapure water, so the discharge state is relatively poor due to immersion processing and manual control.

The WLI and SEM measurement results of the machining results of copper and brass are shown in Fig. 20 and Fig. 21. Fig. 21 and the comparison between Fig. 16(a), (b) and Fig. 20 show that the craters generated in ultrapure water are slightly smaller than those in EDM oil, and the surface roughness Ra is slightly higher than those in EDM oil. This is also consistent with previous research [43]. The reason is that the expansion of the plasma channel in ultrapure water is more limited, so the plasma channel has a higher energy density than that in EDM oil.

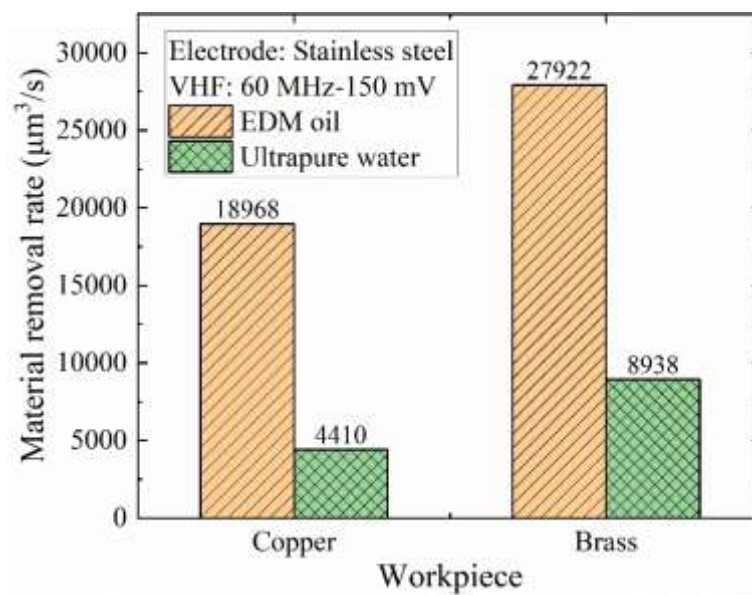


Fig. 19 MRR with different workpiece materials and dielectric fluids.

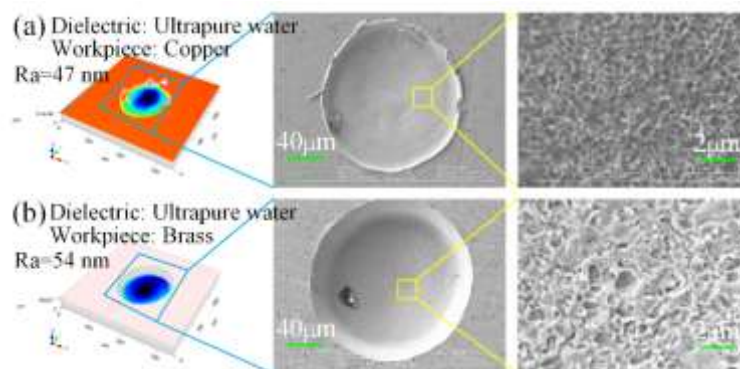


Fig. 20 WLI and SEM images of different workpieces machined in ultrapure water: (a) copper and (b) brass.

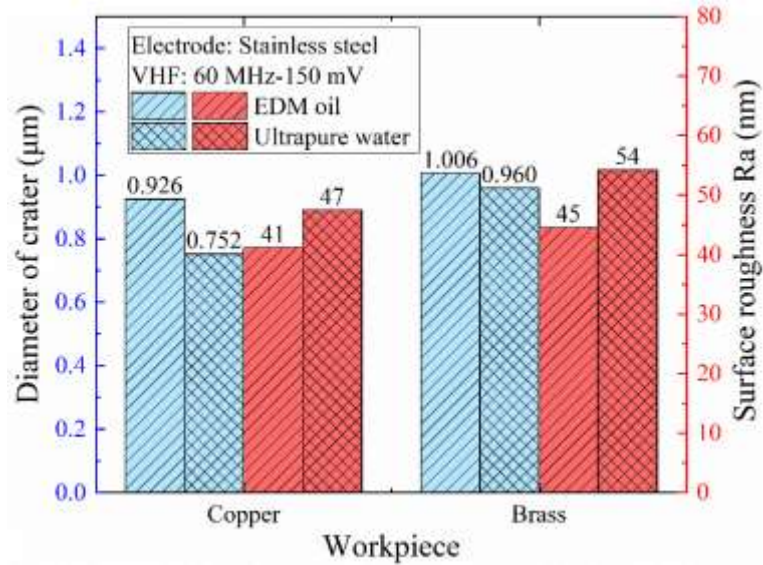


Fig. 21 Diameter of crater and Ra with different workpiece materials and dielectric fluids.

6. Conclusions

In this work, the VHF pulse generator was upgraded. The frequency range of the RF power amplifier was expanded to 110 MHz. The power of the RF power amplifier was also greatly increased, reaching 91 W. The principle of the VHF pulse generator was discussed in detail, and an electro-thermal model that is suitable for VHF micro-EDM was established. The experiments of VHF micro-EDM were carried out. The following conclusions can be drawn from the results:

- (1) Based on the established electro-thermal model of VHF micro-EDM, the reverse solution was done according to the actual machining measurement results. Therefore, the diameter of the plasma channel and the ratio of the workpiece material removal power to the total power were calculated to reveal the mechanism of VHF micro-EDM.
- (2) Discharge experiments were carried out for the key processing parameters of VHF micro-EDM machining, which are the power and frequency of the VHF pulse generator. The effects of power and frequency on machining characteristics were analysed and discussed. At the same frequency, the higher the power is, the higher the MRR is and the larger the number of discharge craters. At the same power, the MRR and the size of discharge craters both first increase and then decrease with increasing frequency and reach the maximum value at 65 MHz. For the copper workpiece in this paper, when the frequency is 110 MHz and the total power of the power amplifier is 8.0 W, 5.6% of the energy is used for the material removal of the workpiece, and the finest processing surface is obtained, for which the surface roughness Ra is as low as 12 nm. The average diameter of the discharge craters is as low as 0.268 μm, and the diameter of the plasma channel is only 0.350 μm. When the frequency is 65 MHz and the total power is 8.0 W, it is at the resonance point and 27.58% of the energy is used for the material removal of the workpiece. The surface roughness Ra

is 58 nm, the average diameter of the discharge craters is only 0.784 μm , and the diameter of the plasma channel is 0.834 μm .

- (3) Discharge experiments for different workpiece materials were also carried out, which prove that the erosion mechanism of VHF micro-EDM is consistent with the traditional micro-EDM theory, and the thermal physical properties of the material determine the difficulty of discharge erosion. Due to the bipolar pulse of the VHF pulse generator, the TWR has no obvious polarity effect in VHF micro-EDM, which is mainly related to the physical properties of the two materials. Finally, the erosion ability in ultrapure water of VHF micro-EDM was also verified.

The detection and control method for VHF micro-EDM is also under study. Furthermore, VHF micro-EDM with a unidirectional pulse is also under development to avoid the relatively high electrode wear caused by the bidirectional pulse. By adjusting the frequency and power of VHF micro-EDM, the proposed machining technology can not only be used for the surface polishing of complex microstructures or 3D printing metal parts but can also meet the high-quality machining requirements of difficult-to-machine metal materials.

Declarations

Ethical Approval The manuscript in part or in full has not been submitted or published anywhere, and the manuscript will not be submitted elsewhere until the editorial process is completed.

Consent to Participate Approved.

Consent to Publish Approved.

Authors Contributions Qi Jing is responsible for Concept, Experiment, Paper draft; Yongbin Zhang is responsible for Funding acquisition, Supervision; Lingbao Kong is responsible for Paper revision, Supervision, Funding acquisition; Min Xu is responsible for Supervision, Funding acquisition; Fang Ji is responsible for Supervision.

Funding Science Challenging Program of CAEP (JDZZ2016006-0104), Natural Science Foundation of China (52075100), Shanghai Science and Technology Committee Innovation Grant (19ZR1404600), Innovation and Development Funding Project of CAEP (K1173), and Key R&D Program of Sichuan Province of China (21ZDYF3793).

Competing Interests The authors declare no competing interests.

Availability of data and materials Data and materials used in this research are available.

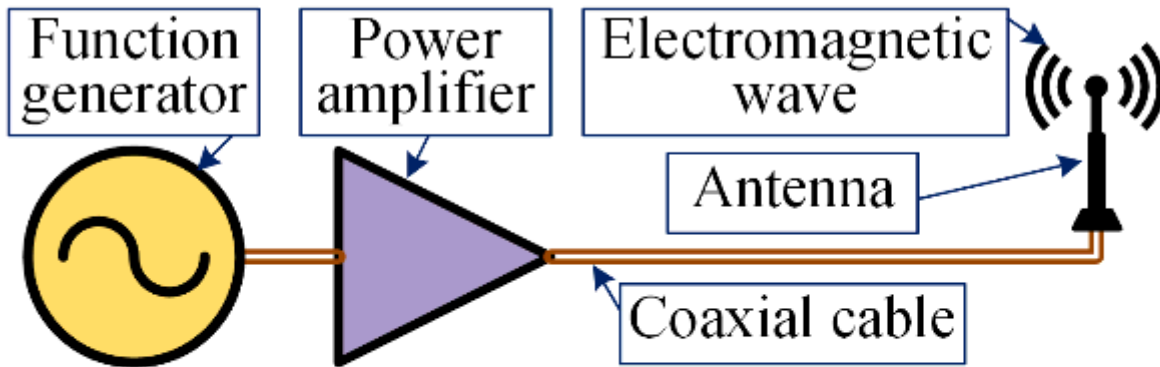
References

- [1] Oliaei SNB, Karpat Y, Davim JP, Perveen A. (2018) Micro tool design and fabrication: A review. *Journal of Manufacturing Processes*,36:496-519. doi: 10.1016/j.jmapro.2018.10.038
- [2] Chavoshi SZ, Luo X. (2015) Hybrid micro-machining processes: A review. *Precision Engineering*,41:1-23. doi: 10.1016/j.precisioneng.2015.03.001
- [3] Shin Y, Barnett LR, Gamzina D, Luhmann NC, Field M, Borwick R. (2009) Terahertz vacuum electronic circuits fabricated by UV lithographic molding and deep reactive ion etching. *Applied Physics Letters*,95:181505. doi: 10.1063/1.3259823
- [4] Chua C, Tsai JM, Aditya S, Tang M, Ho SW, Shen Z, Wang L. (2011) Microfabrication and Characterization of W-Band Planar Helix Slow-Wave Structure With Straight-Edge Connections. *IEEE Transactions on Electron Devices*,58:4098-4105. doi: 10.1109/TED.2011.2165284
- [5] Hu P, Lei W, Jiang Y, Huang Y, Song R, Chen H, Dong Y. (2018) Development of a 0.32-THz Folded Waveguide Traveling Wave Tube. *IEEE Transactions on Electron Devices*,65:2164-2169. doi: 10.1109/TED.2017.2787682
- [6] Li CJ, Li Y, Tong H, Zhao L, Kong QC, Wang ZQ. (2016) An EDM pulse power generator and its feasible experiments for drilling film cooling holes. *The International Journal of Advanced Manufacturing Technology*,87:1813-1821. doi: 10.1007/s00170-016-8598-0
- [7] Hourmand M, Sarhan AAD, Sayuti M. (2017) Micro-electrode fabrication processes for micro-EDM drilling and milling: a state-of-the-art review. *The International Journal of Advanced Manufacturing Technology*,91:1023-1056. doi: 10.1007/s00170-016-9671-4
- [8] Rahman M, Asad ABMA, Masaki T, Saleh T, Wong YS, Senthil Kumar A. (2010) A multiprocess machine tool for compound micromachining. *International Journal of Machine Tools and Manufacture*,50:344-356. doi: 10.1016/j.ijmachtools.2009.10.007
- [9] Klocke F, Schneider S, Ehle L, Meyer H, Hensgen L, Klink A. (2016) Investigations on Surface Integrity of Heat Treated 42CrMo4 (AISI 4140) Processed by Sinking EDM. *Procedia CIRP*,42:580-585. doi: 10.1016/j.procir.2016.02.263
- [10] Sari D, Welling D, Löpenhaus C, Klocke F, Klink A. (2016) Adjusting Surface Integrity of Gears Using Wire EDM to Increase the Flank Load Carrying Capacity. *Procedia CIRP*,45:295-298. doi: 10.1016/j.procir.2016.02.355
- [11] Shen Y, Liu Y, Dong H, Zhang K, Lv L, Zhang X, Wu X, et al. (2017) Surface integrity of Inconel 718 in high-speed electrical discharge machining milling using air dielectric. *The International Journal of Advanced Manufacturing Technology*,90:691-698. doi: 10.1007/s00170-016-9332-7
- [12] Maity KP, Singh RK. (2012) An optimisation of micro-EDM operation for fabrication of micro-hole. *The International Journal of Advanced Manufacturing Technology*,61:1221-1229. doi: 10.1007/s00170-012-4098-z
- [13] Tong H, Li Y, Wang Y, Yu D. (2008) Servo scanning 3D micro-EDM based on macro/micro-dual-feed spindle. *International Journal of Machine Tools and Manufacture*,48:858-869. doi: 10.1016/j.ijmachtools.2007.11.008
- [14] Fu XZ, Zhang Y, Zhang QH, Zhang JH. (2013) Research on Piezoelectric Self-Adaptive Micro-EDM. *Procedia CIRP*,6:303-308. doi: 10.1016/j.procir.2013.03.034
- [15] Qian J, Yang F, Wang J, Lauwers B, Reynaerts D. (2015) Material removal mechanism in low-energy micro-EDM process. *CIRP Annals*,64:225-228. doi: 10.1016/j.cirp.2015.04.040

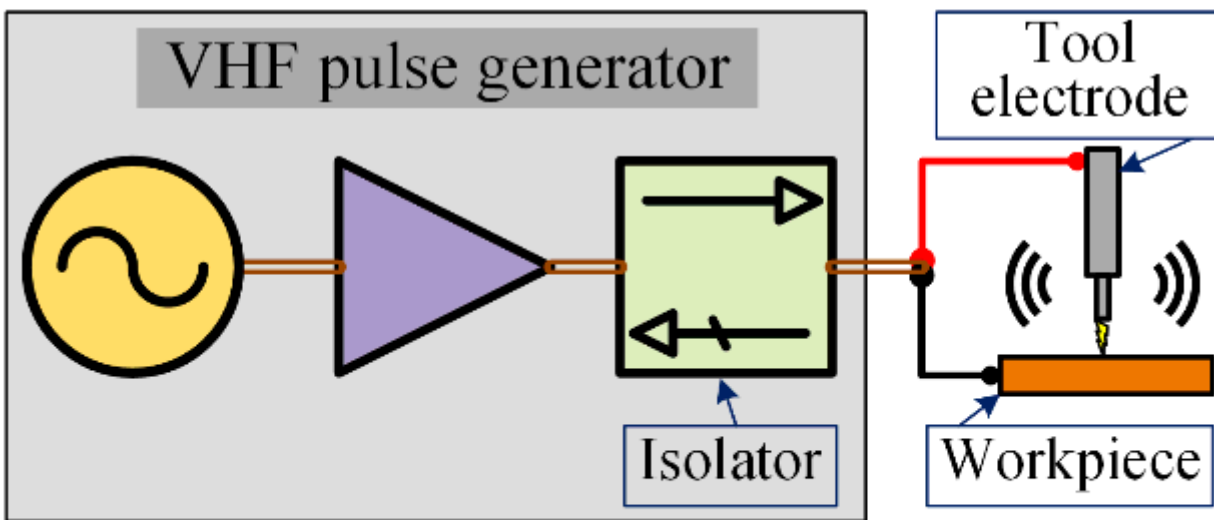
- [16] Nguyen MD, Rahman M, Wong YS. (2013) Transitions of micro-EDM/SEDCM/micro-ECM milling in low-resistivity deionized water. *International Journal of Machine Tools and Manufacture*,69:48-56. doi: 10.1016/j.ijmachtools.2013.03.008
- [17] Zeng Z, Wang Y, Wang Z, Shan D, He X. (2012) A study of micro-EDM and micro-ECM combined milling for 3D metallic micro-structures. *Precision Engineering*,36:500-509. doi: 10.1016/j.precisioneng.2012.01.005
- [18] Chu X, Zhuang W, Xue W, Quan X, Zhou W, Fu T. (2020) Electrolytic removal of recast layers on micro-EDM microstructure surfaces. *The International Journal of Advanced Manufacturing Technology*,108:867-879. doi: 10.1007/s00170-020-05410-x
- [19] Bissacco G, Hansen HN, Tristo G, Valentincic J. (2011) Feasibility of wear compensation in micro EDM milling based on discharge counting and discharge population characterization. *CIRP Annals*,60:231-234. doi: 10.1016/j.cirp.2011.03.064
- [20] Egashira K, Matsugasako A, Tsuchiya H, Miyazaki M. (2006) Electrical discharge machining with ultralow discharge energy. *Precision Engineering*,30:414-420. doi: 10.1016/j.precisioneng.2006.01.004
- [21] Jahan MP, Wong YS, Rahman M. (2009) A study on the quality micro-hole machining of tungsten carbide by micro-EDM process using transistor and RC-type pulse generator. *Journal of Materials Processing Technology*,209:1706-1716. doi: 10.1016/j.jmatprotec.2008.04.029
- [22] Yang F, Bellotti M, Hua H, Yang J, Qian J, Reynaerts D. (2018) Experimental analysis of normal spark discharge voltage and current with a RC-type generator in micro-EDM. *The International Journal of Advanced Manufacturing Technology*,96:2963-2972. doi: 10.1007/s00170-018-1813-4
- [23] Han F, Jiang J, Yu D. (2007) Influence of discharge current on machined surfaces by thermo-analysis in finish cut of WEDM. *International Journal of Machine Tools and Manufacture*,47:1187-1196. doi: 10.1016/j.ijmachtools.2006.08.024
- [24] Chu X, Feng W, Wang C, Hong Y. (2017) Analysis of mechanism based on two types of pulse generators in micro-EDM using single pulse discharge. *The International Journal of Advanced Manufacturing Technology*,89:3217-3230. doi: 10.1007/s00170-016-9287-8
- [25] Kunieda M, Hayasaka A, Yang XD, Sano S, Araie I. (2007) Study on Nano EDM Using Capacity Coupled Pulse Generator. *CIRP Annals*,56:213-216. doi: 10.1016/j.cirp.2007.05.051
- [26] Okada A, McGeough JA, MacMillan D, Flynn B. (2006) Machining Characteristics of EDM by Radio-frequency Plasma. *CIRP Annals - Manufacturing Technology*,55:167-170. doi: 10.1016/S0007-8506(07)60390-4
- [27] Khattak HK, Bianucci P, Slepko AD. (2019) Linking plasma formation in grapes to microwave resonances of aqueous dimers. *Proceedings of the National Academy of Sciences*,116:4000-4005. doi: 10.1073/pnas.1818350116
- [28] Wang F, Zhang Y, Liu G, Wang Q. (2019) Improvement of processing quality based on VHF resonant micro-EDM pulse generator. *The International Journal of Advanced Manufacturing Technology*,104:3663-3677. doi: 10.1007/s00170-019-03896-8
- [29] Zhang Y, Liu Y, Shen Y, Li Z, Ji R, Cai B. (2014) A novel method of determining energy distribution and plasma diameter of EDM. *International Journal of Heat and Mass Transfer*,75:425-432. doi: 10.1016/j.ijheatmasstransfer.2014.03.082
- [30] Wang K, Zhang Q, Zhu G, Liu Q, Huang Y, Zhang J. (2017) Research on the energy distribution of micro EDM by utilization of electro-thermal model. *The International Journal of Advanced*

- Manufacturing Technology,93:4179-4186. doi: 10.1007/s00170-017-0822-z
- [31] Singh H. (2012) Experimental study of distribution of energy during EDM process for utilization in thermal models. *International Journal of Heat and Mass Transfer*,55:5053-5064. doi: 10.1016/j.ijheatmasstransfer.2012.05.004
- [32] Assarzadeh S, Ghoreishi M. (2017) Prediction of root mean square surface roughness in low discharge energy die-sinking EDM process considering the effects of successive discharges and plasma flushing efficiency. *Journal of Manufacturing Processes*,30:502-515. doi: <https://doi.org/10.1016/j.jmapro.2017.10.012>
- [33] Shabgard M, Ahmadi R, Seyedzavvar M, Oliaei SNB. (2013) Mathematical and numerical modeling of the effect of input-parameters on the flushing efficiency of plasma channel in EDM process. *International Journal of Machine Tools and Manufacture*,65:79-87. doi: 10.1016/j.ijmachtools.2012.10.004
- [34] Fazli Shahri HR, Mahdavinejad R, Ashjaee M, Abdullah A. (2017) A comparative investigation on temperature distribution in electric discharge machining process through analytical, numerical and experimental methods. *International Journal of Machine Tools and Manufacture*,114:35-53. doi: 10.1016/j.ijmachtools.2016.12.005
- [35] Hinduja S, Kunieda M. (2013) Modelling of ECM and EDM processes. *CIRP Annals*,62:775-797. doi: 10.1016/j.cirp.2013.05.011
- [36] ZAHIRUDDIN M, KUNIEDA M. (2010) Energy Distribution Ratio into Micro EDM Electrodes. *Journal of Advanced Mechanical Design, Systems, and Manufacturing*,4:1095-1106. doi: 10.1299/jamdsm.4.1095
- [37] Kiran MPSK, Joshi SS. (2007) Modeling of surface roughness and the role of debris in micro-EDM. *JOURNAL OF MANUFACTURING SCIENCE AND ENGINEERING-TRANSACTIONS OF THE ASME*,129:265-273. doi: 10.1115/1.2540683
- [38] Zhang QH, Du R, Zhang JH, Zhang QB. (2006) An investigation of ultrasonic-assisted electrical discharge machining in gas. *International Journal of Machine Tools and Manufacture*,46:1582-1588. doi: 10.1016/j.ijmachtools.2005.09.023
- [39] Salonitis K, Stournaras A, Stavropoulos P, Chryssolouris G. (2009) Thermal modeling of the material removal rate and surface roughness for die-sinking EDM. *The International Journal of Advanced Manufacturing Technology*,40:316-323. doi: 10.1007/s00170-007-1327-y
- [40] Wang R, Duan W, Wang K, Dong X, Fan Z, Mei X, Wang W, et al. (2018) Computational and experimental study on hole evolution and delamination in laser drilling of thermal barrier coated nickel superalloy. *Optics and Lasers in Engineering*,107:161-175. doi: 10.1016/j.optlaseng.2018.03.019
- [41] Chakraborty S, Dey V, Ghosh SK. (2015) A review on the use of dielectric fluids and their effects in electrical discharge machining characteristics. *Precision Engineering*,40:1-6. doi: 10.1016/j.precisioneng.2014.11.003
- [42] Wu Z, Luo F, Guo D, Wu X, Xu B, Lei J, Liang X, et al. (2018) Micro-EDM by using laminated 3D microelectrodes with deionized water containing B4C powder. *The International Journal of Advanced Manufacturing Technology*,99:2893-2902. doi: 10.1007/s00170-018-2581-x
- [43] Zhao Y, Kunieda M, Abe K. (2016) Comparison on foil EDM characteristics of single crystal SiC between in deionized water and in EDM oil. *The International Journal of Advanced Manufacturing Technology*,86:2905-2912. doi: 10.1007/s00170-016-8412-z

Figures



(a) VHF system



(b) VHF micro-EDM

Figure 1

Schematic diagram of the (a) VHF transmitting system and (b) VHF micro-EDM.

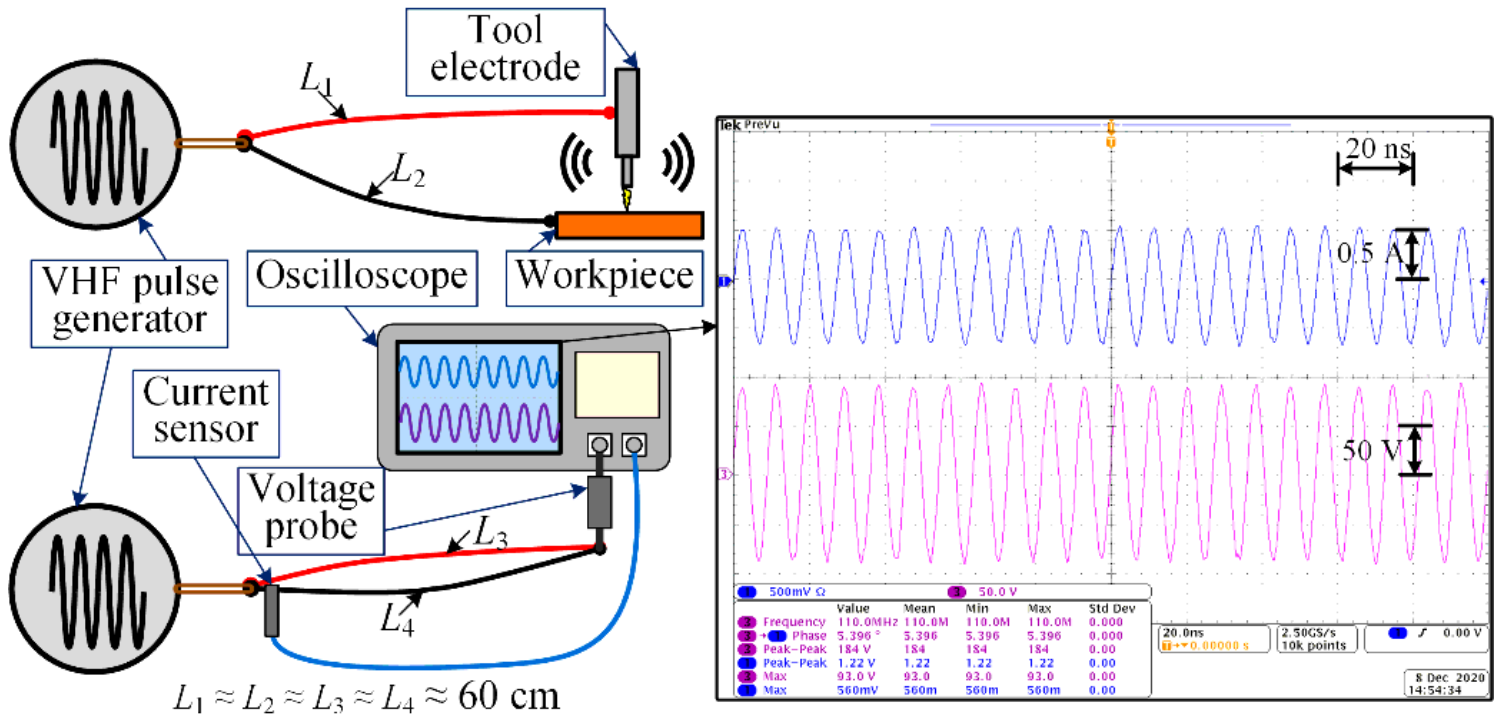


Figure 2

Schematic diagram of the measurement and the voltage and current results.

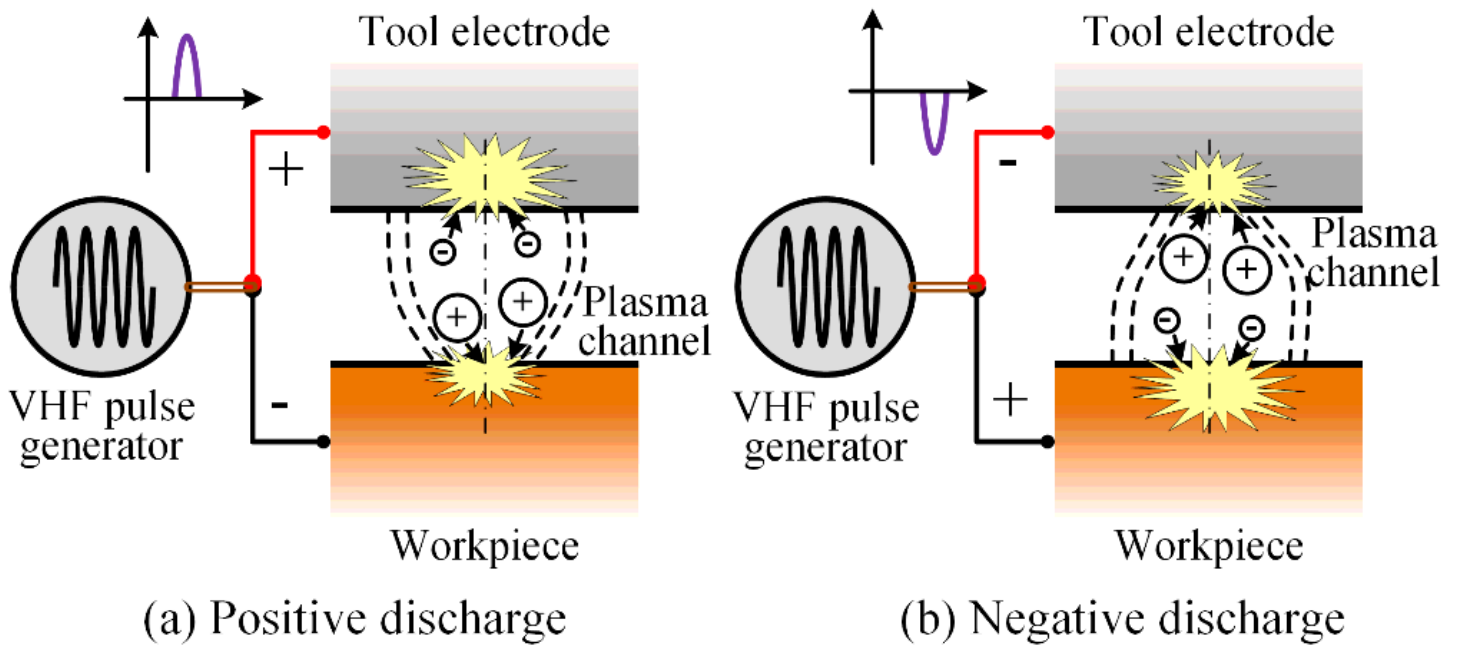


Figure 3

Discharge principle of the VHF pulse generator: (a) positive discharge and (b) negative discharge.

Figure 4

The whole equivalent circuit of VHF micro-EDM.

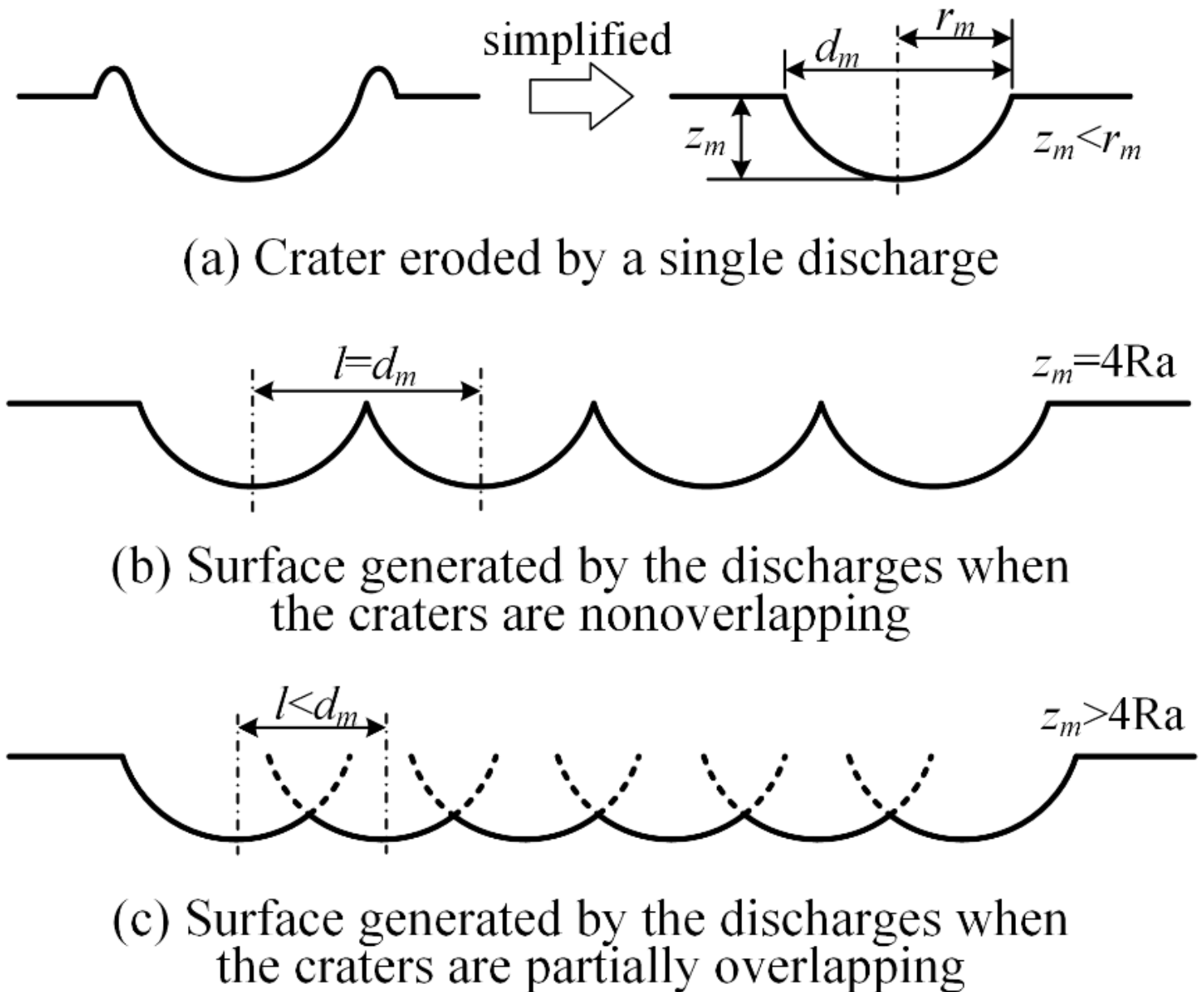


Figure 5

Simplification of the crater: (a) crater eroded by a single discharge, (b) surface generated by the discharges when the craters are nonoverlapping and (c) surface generated by the discharges when the craters are partially overlapping.

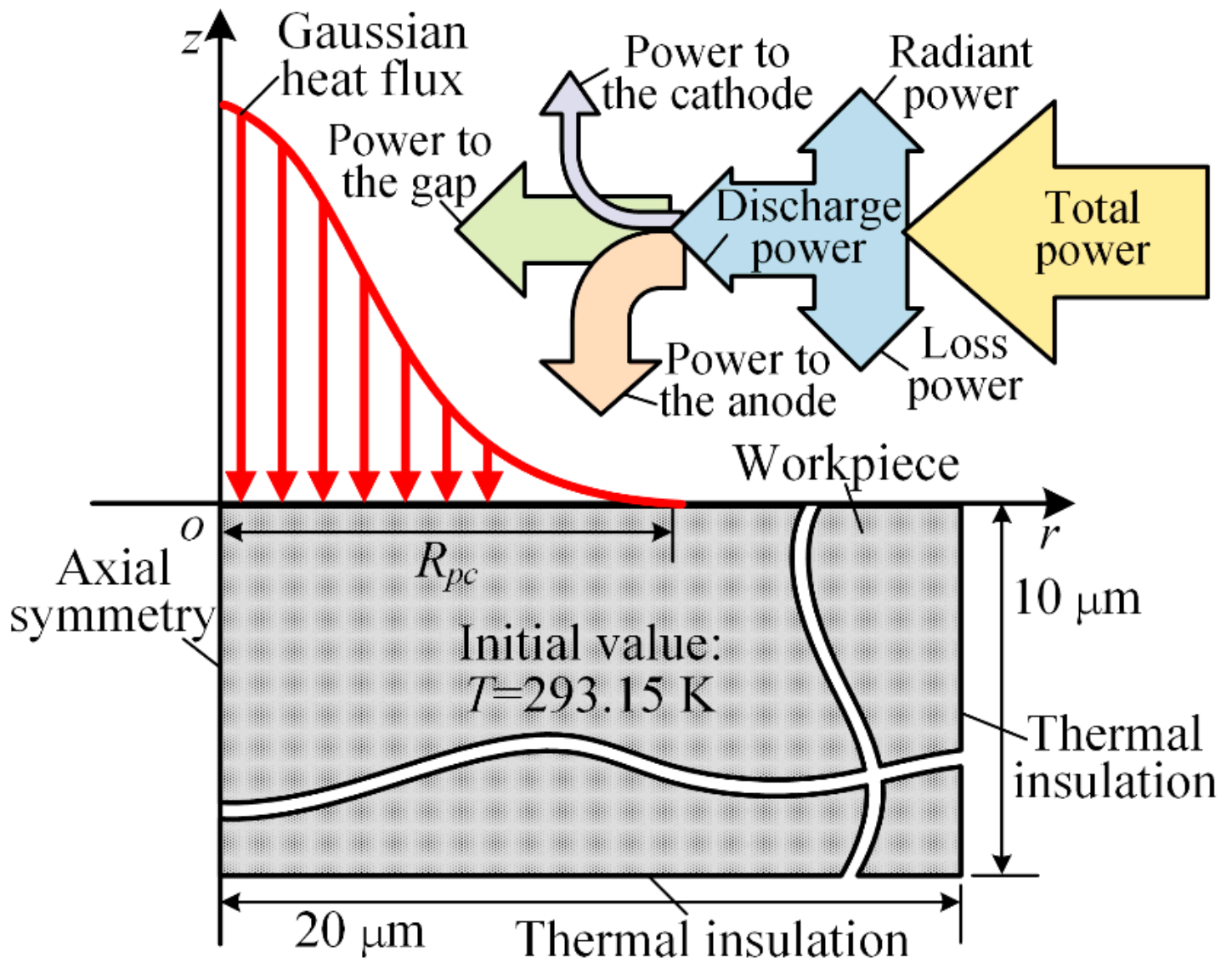


Figure 6

Schematic diagram of simulation model.

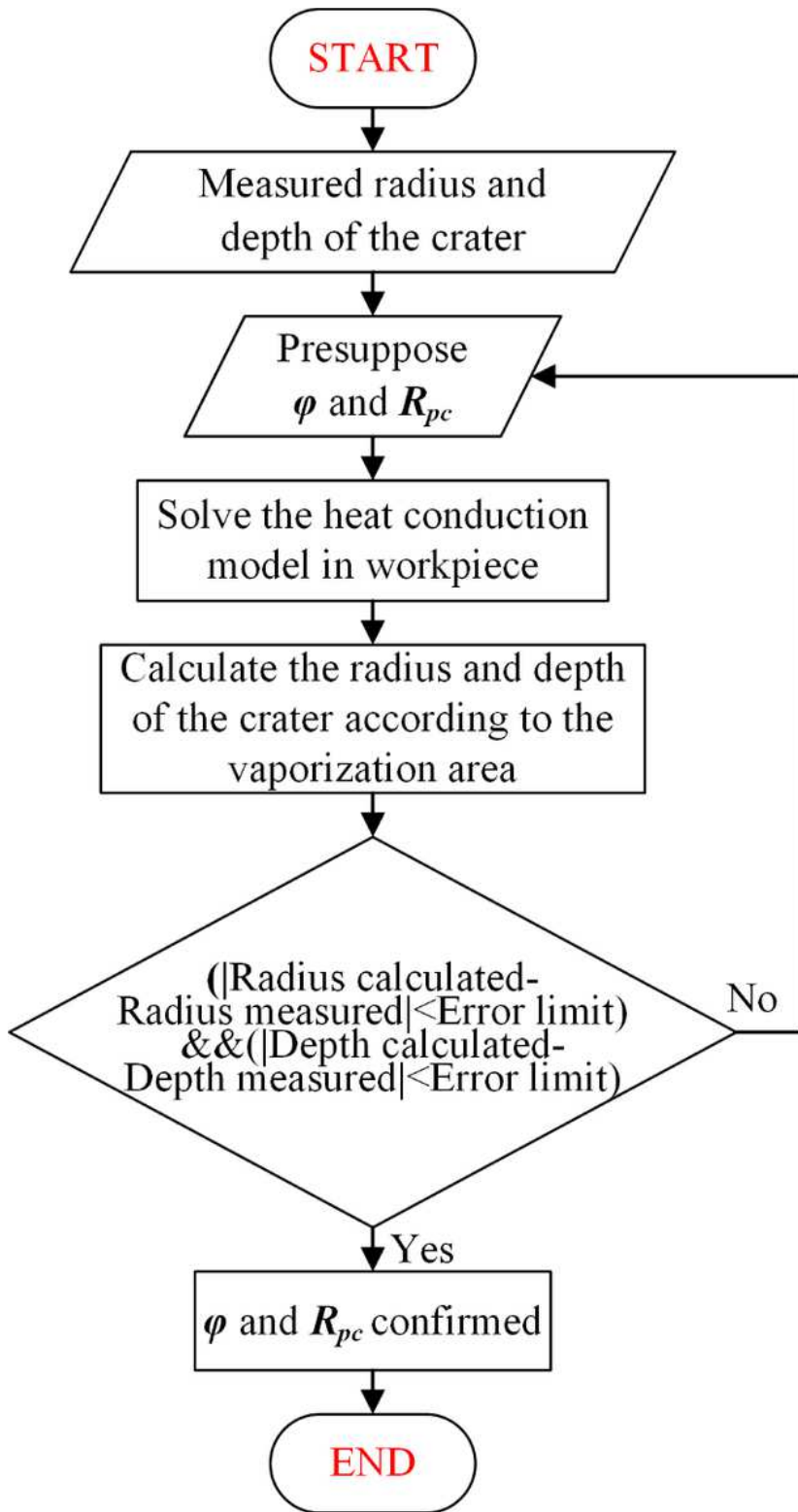


Figure 7

Flowchart of the solution procedure.

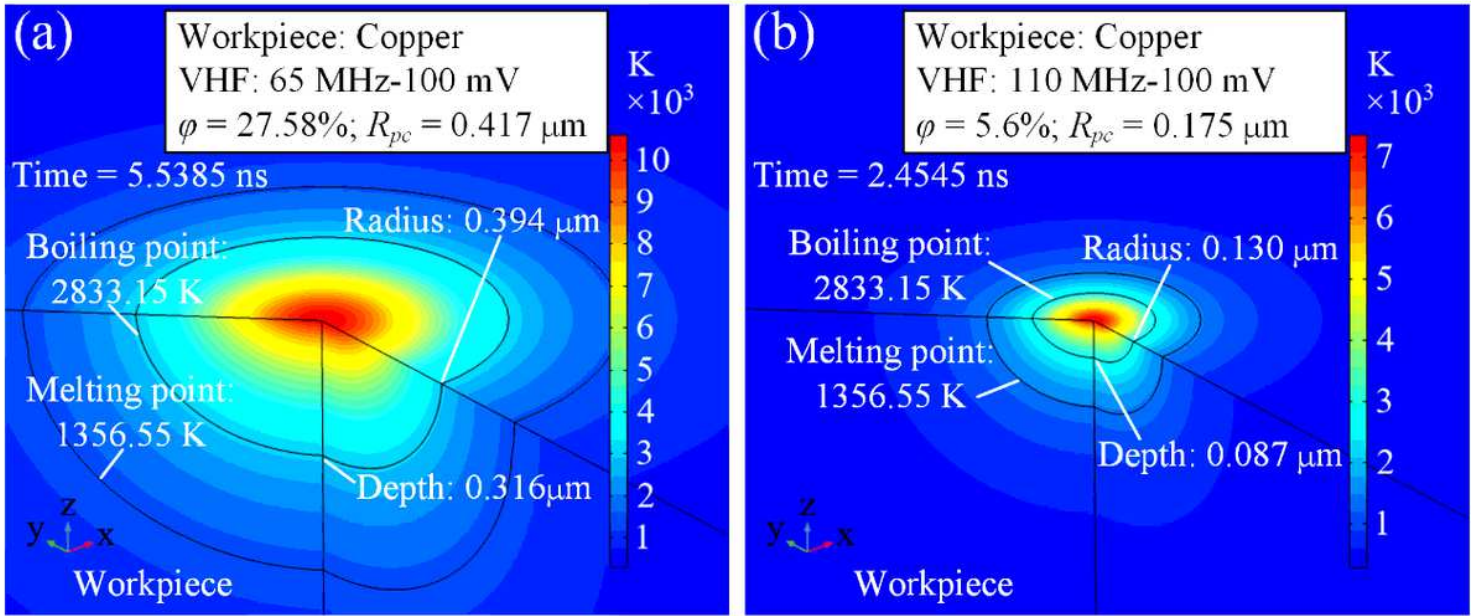


Figure 8

Calculation results of (a) 65 MHz-100 mV and (b) 110 MHz-100 mV.

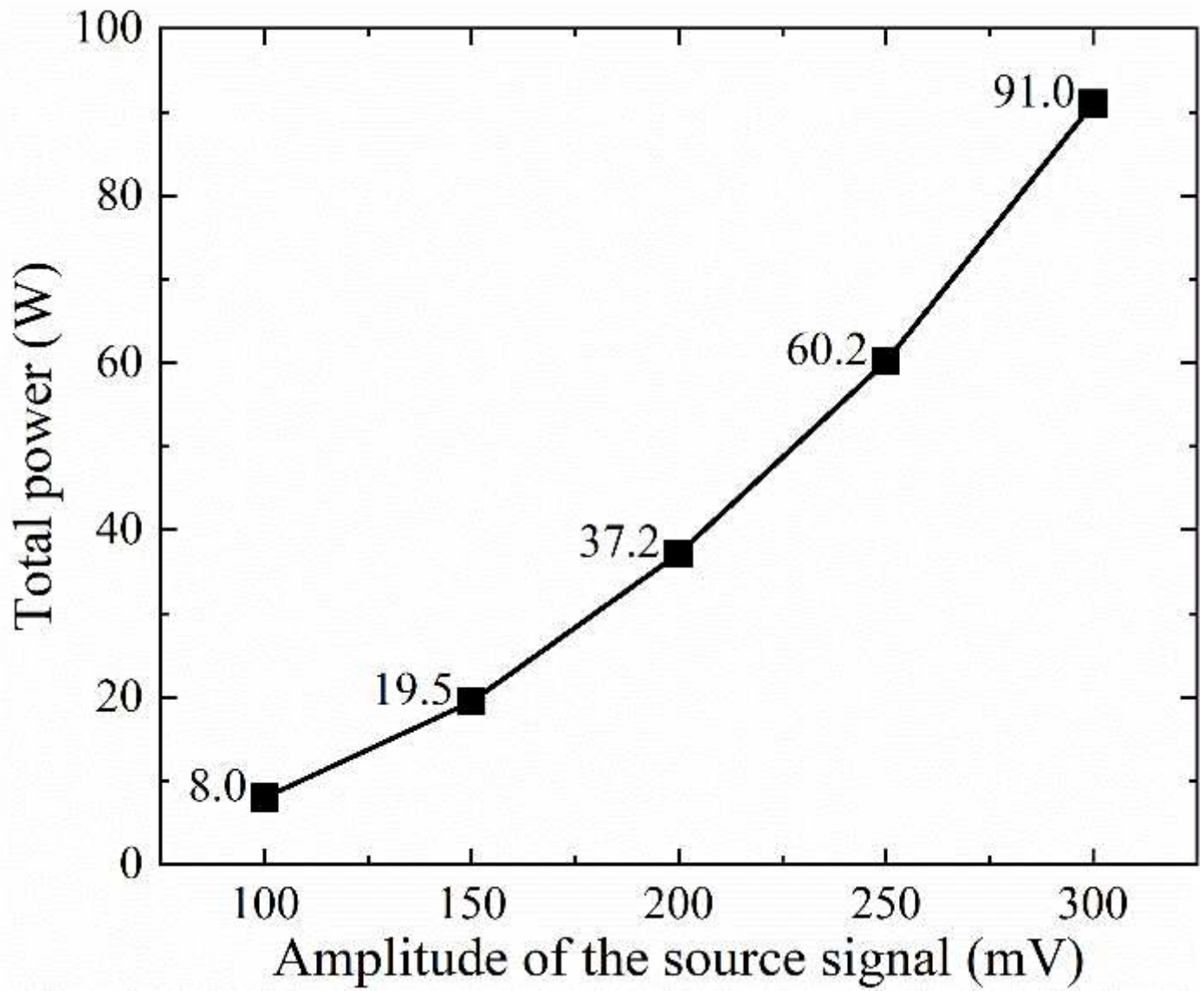


Figure 9

Relation between the total power and the amplitude of the source signal.

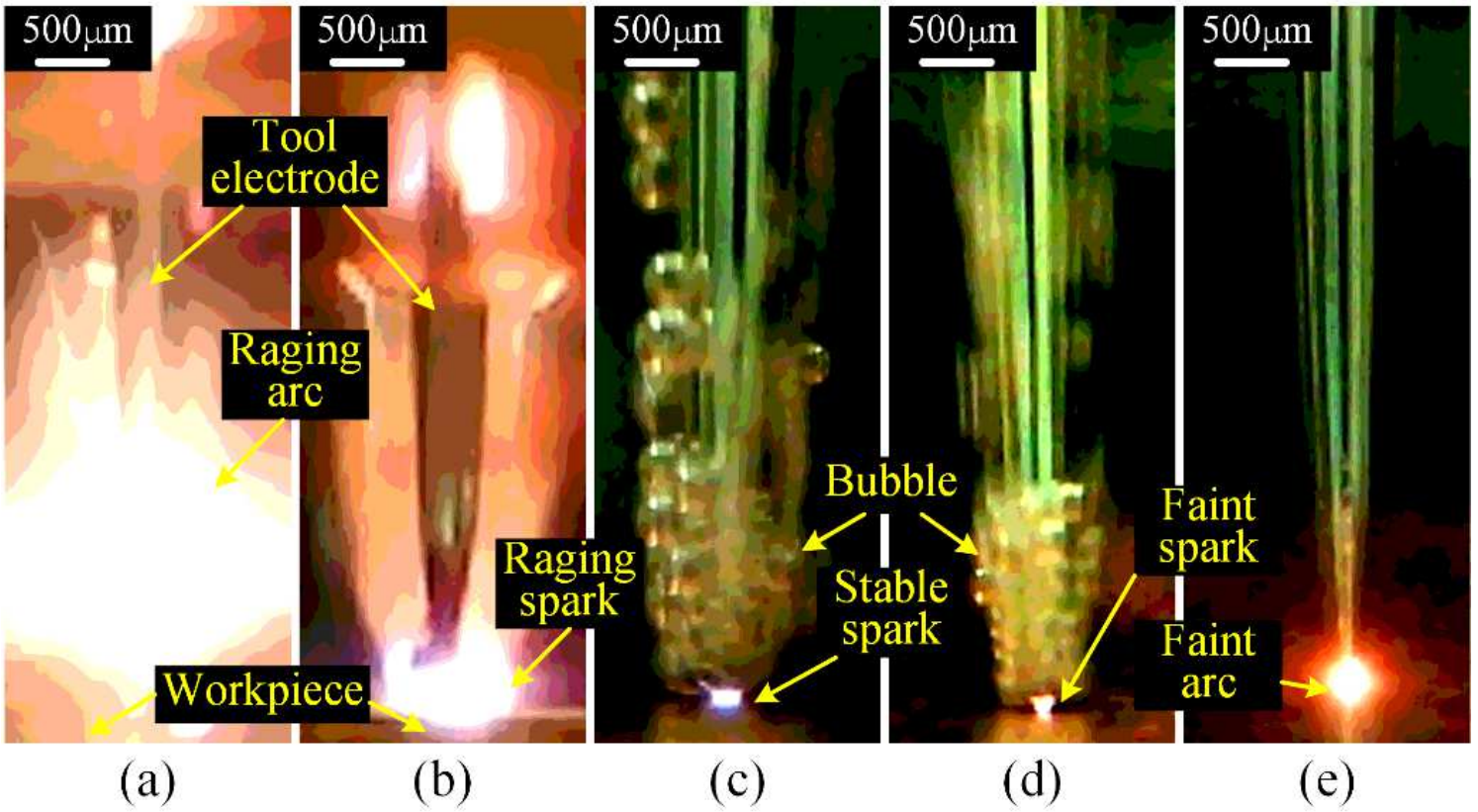


Figure 10

Pictures of the processing in EDM oil under different conditions: (a) 65 MHz-200 mV, (b) 65 MHz-150 mV, (c) 65 MHz-100 mV, (d) 90 MHz-100 mV and (e) 110 MHz-100 mV.

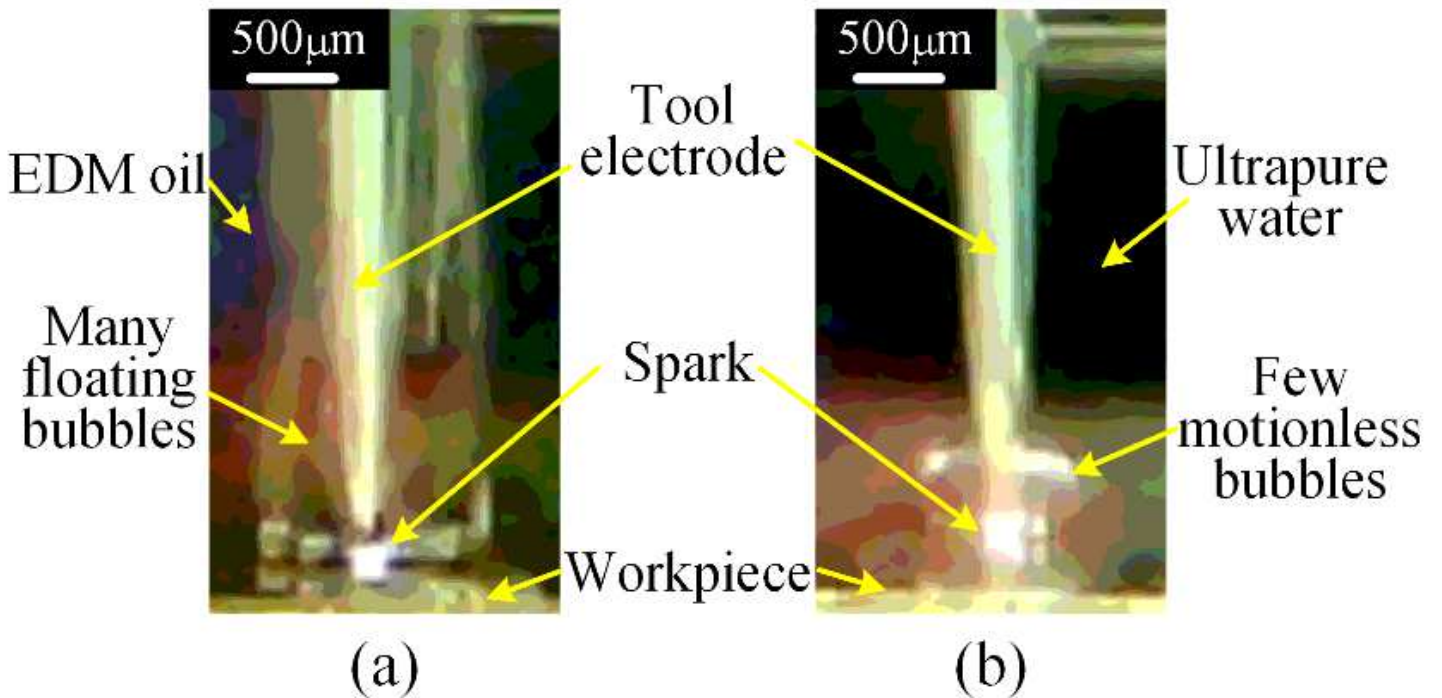


Figure 11

Pictures of the processing under 60 MHz-150 mV in (a) EDM oil and (b) ultrapure water.

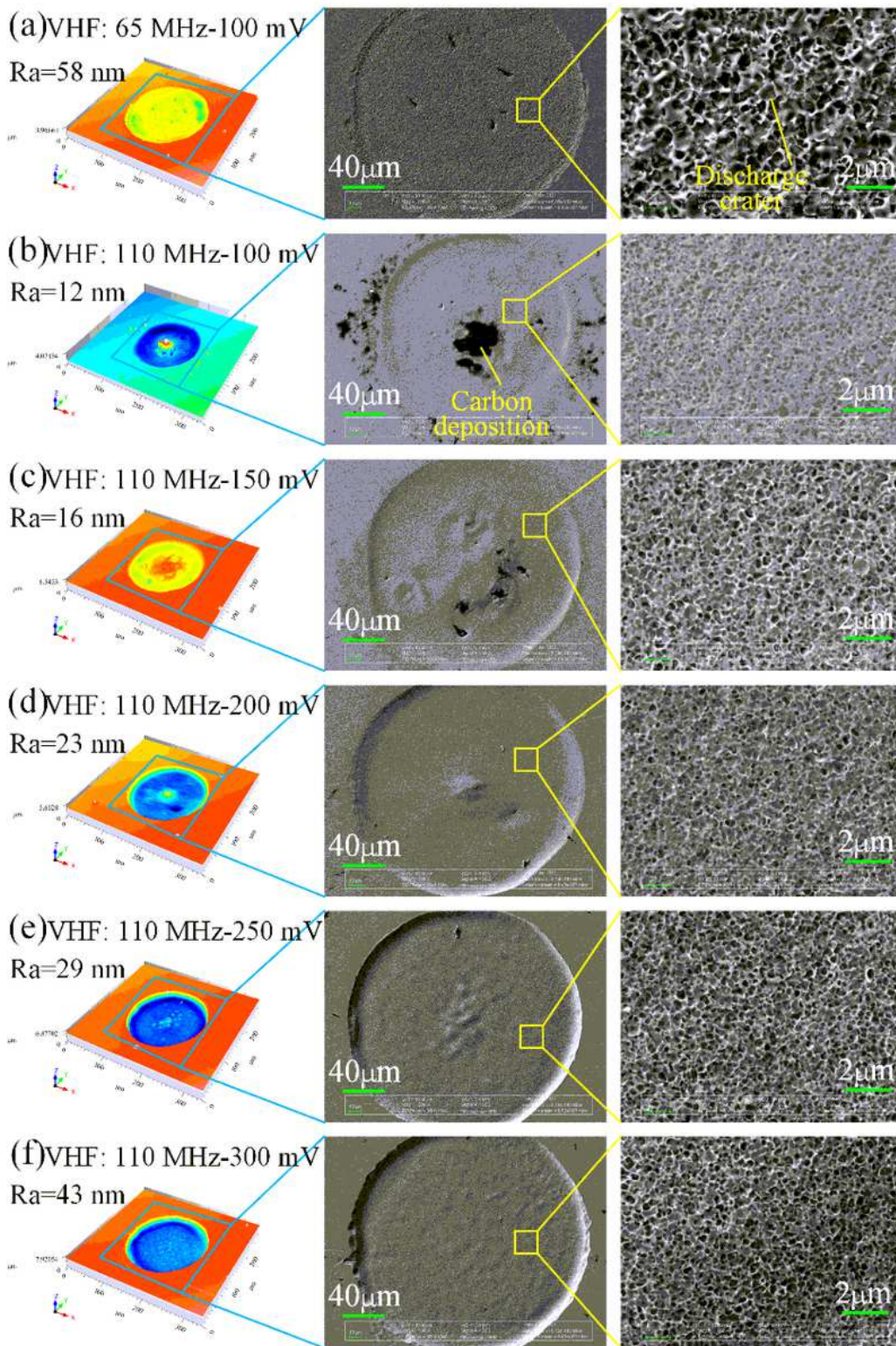


Figure 12

WLI and SEM images of the copper workpiece under (a) 65 MHz-100 mV, (b) 110 MHz-100 mV, (c) 110 MHz-150 mV, (d) 110 MHz-200 mV, (e) 110 MHz-250 mV and (f) 110 MHz-300 mV.

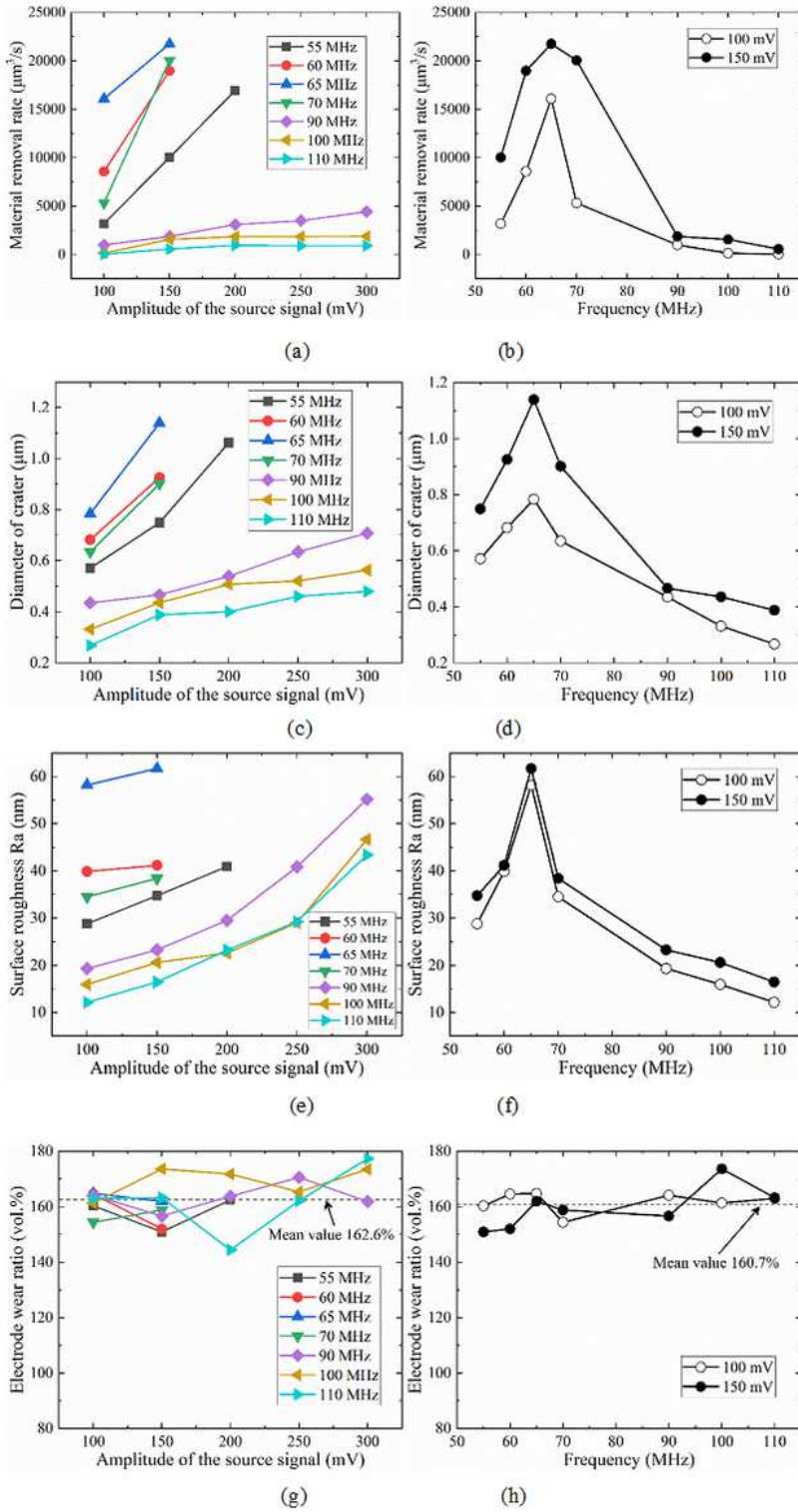


Figure 13

Variation curves of all the processing results with the variation of voltage amplitude of the source signal and frequency: variations of (a) MRR with amplitude, (b) MRR with frequency, (c) diameter of crater with amplitude, (d) diameter of crater with frequency, (e) Ra with amplitude, (f) Ra with frequency, (g) TWR with amplitude and (h) TWR with frequency.

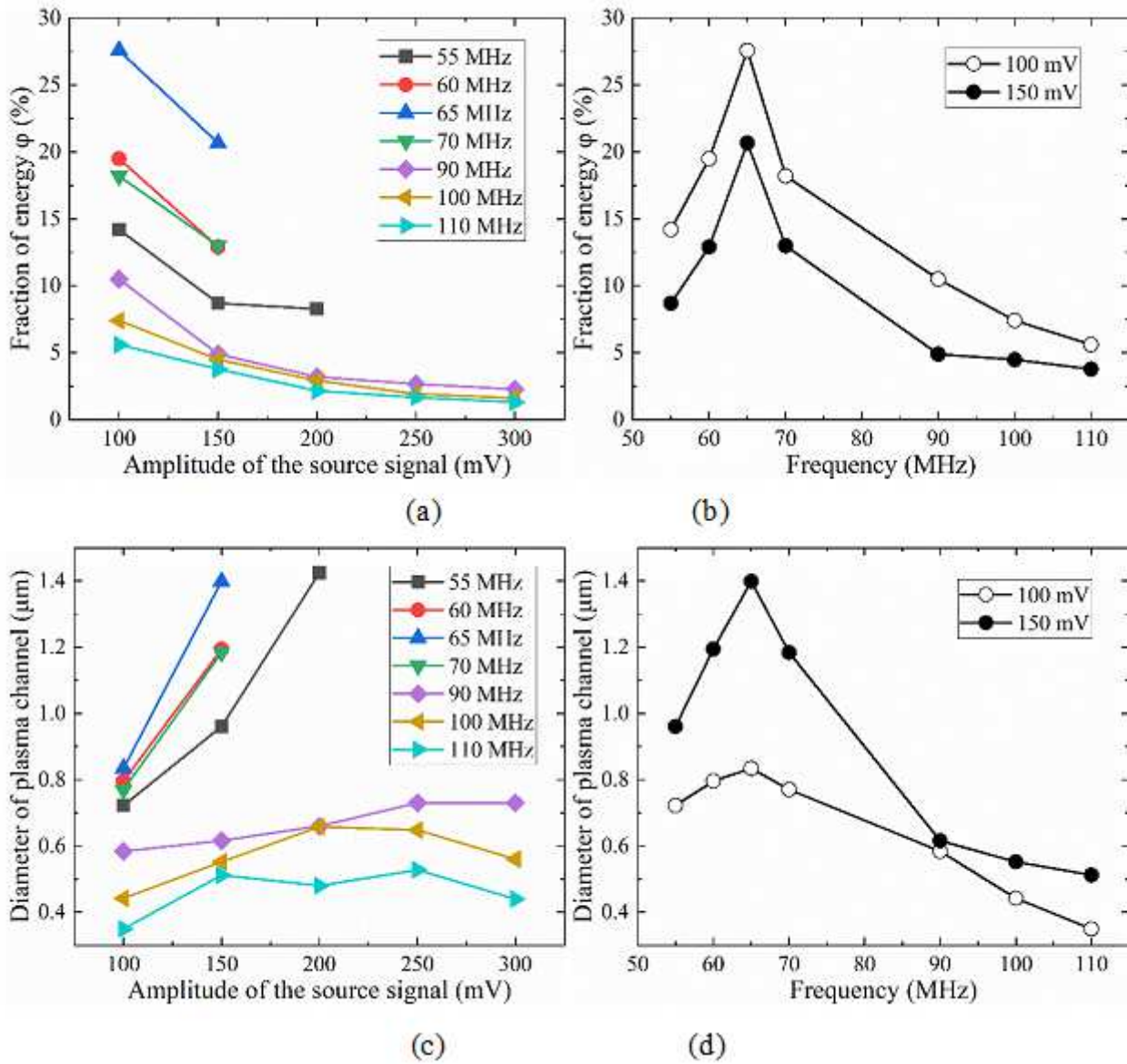


Figure 14

Variation curves of the calculation results with the variation of voltage amplitude of the source signal and frequency: variations of (a) with amplitude, (b) with frequency, (c) diameter of plasma channel with amplitude and (d) diameter of plasma channel with frequency.

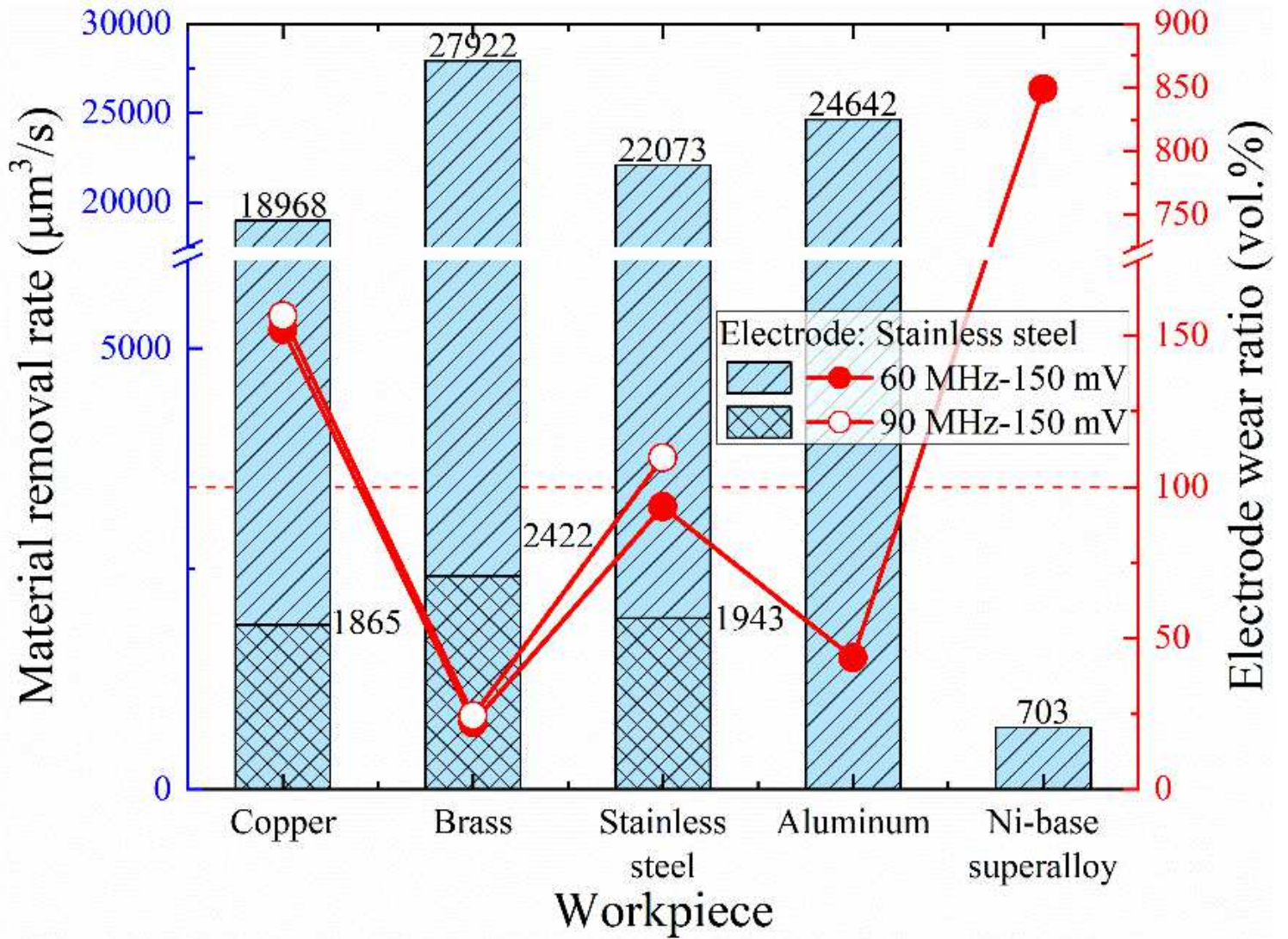


Figure 15

MRR and TWR with different workpiece materials.

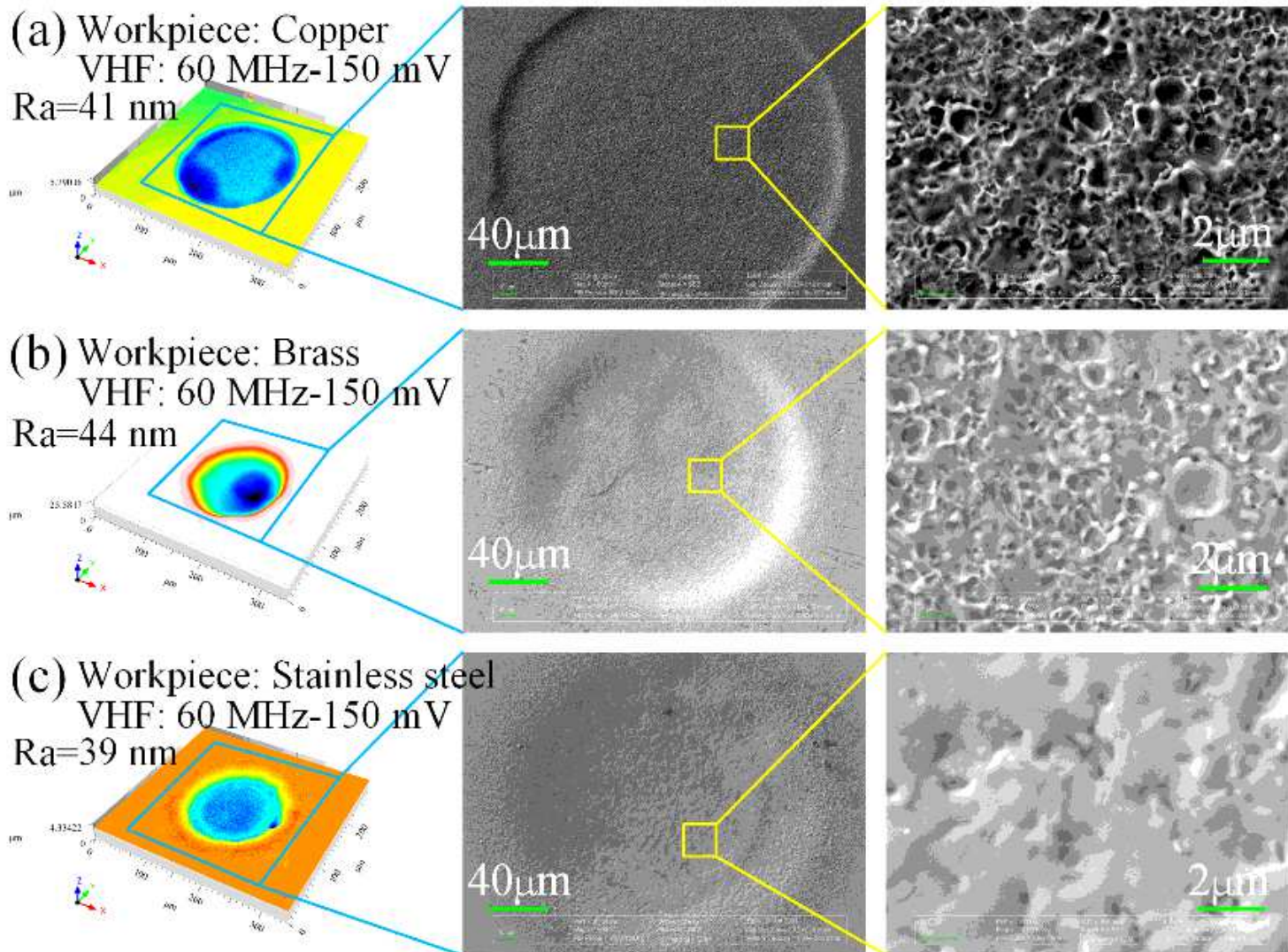


Figure 16

WLI and SEM images of different workpieces under 60 MHz-150 mV: (a) copper, (b) brass and (c) stainless steel.

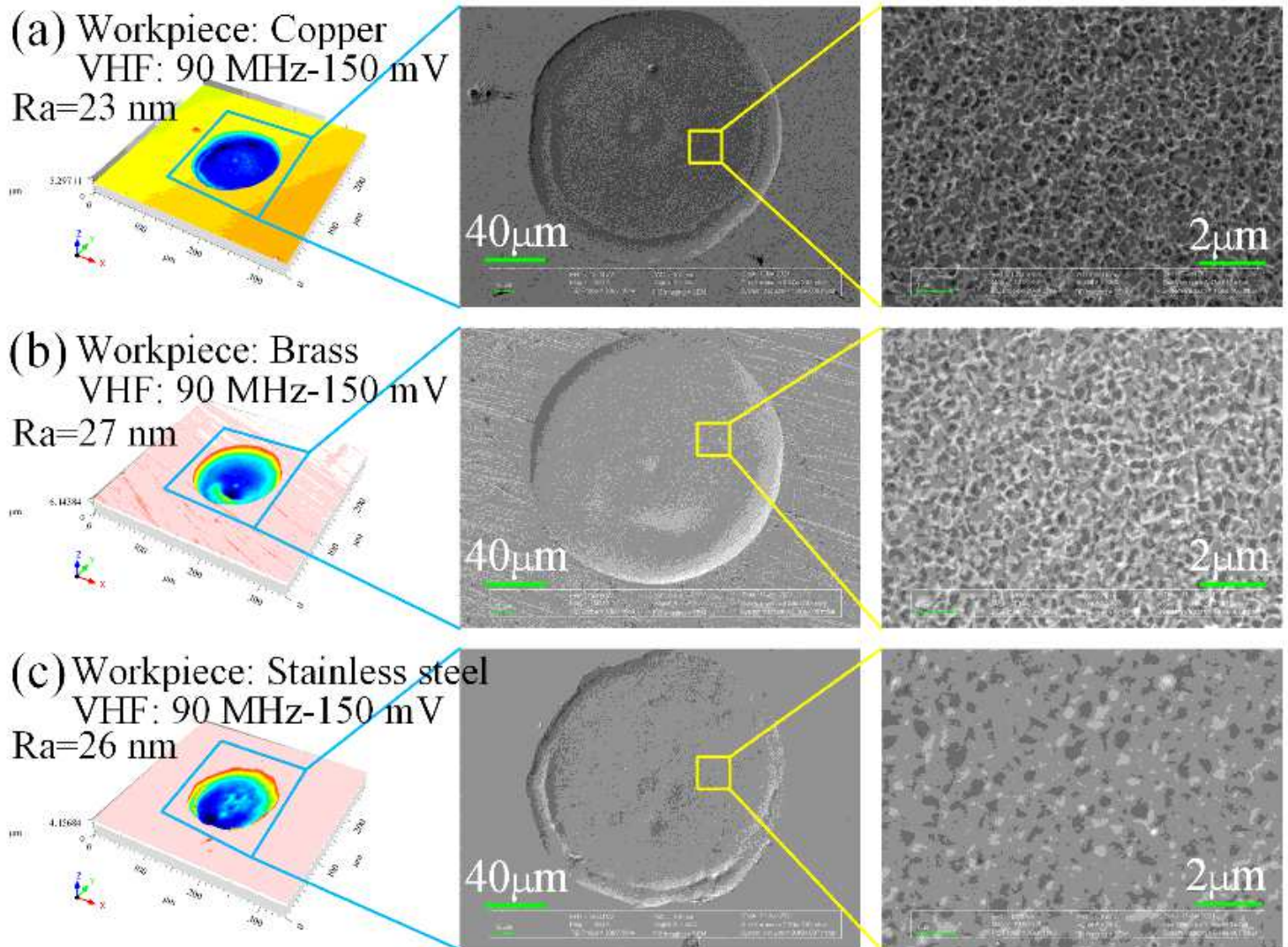


Figure 17

WLI and SEM images of different workpieces under 90 MHz-150 mV: (a) copper, (b) brass and (c) stainless steel.

Figure 18

Diameter of crater and Ra with different workpiece materials.

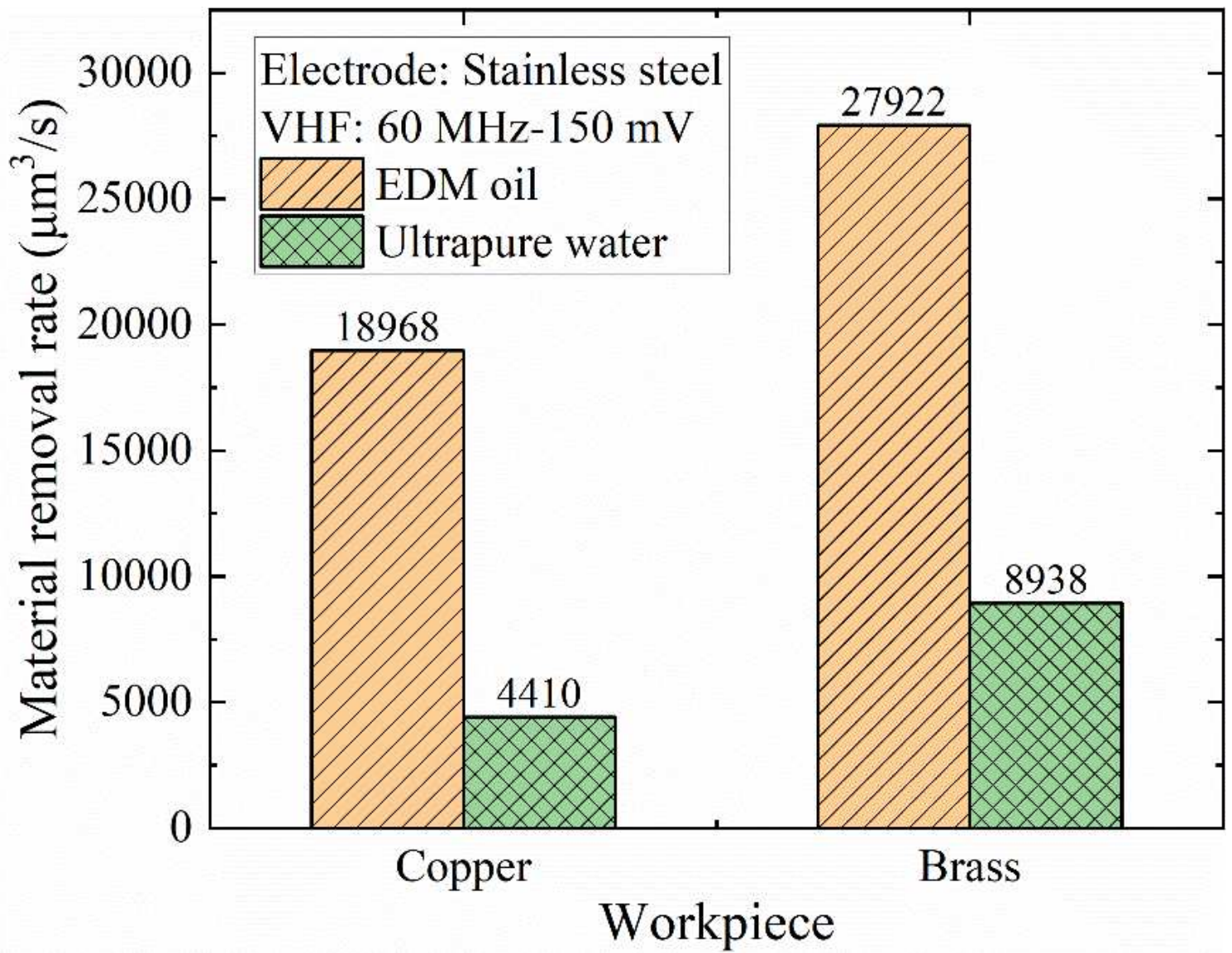


Figure 19

MRR with different workpiece materials and dielectric fluids.

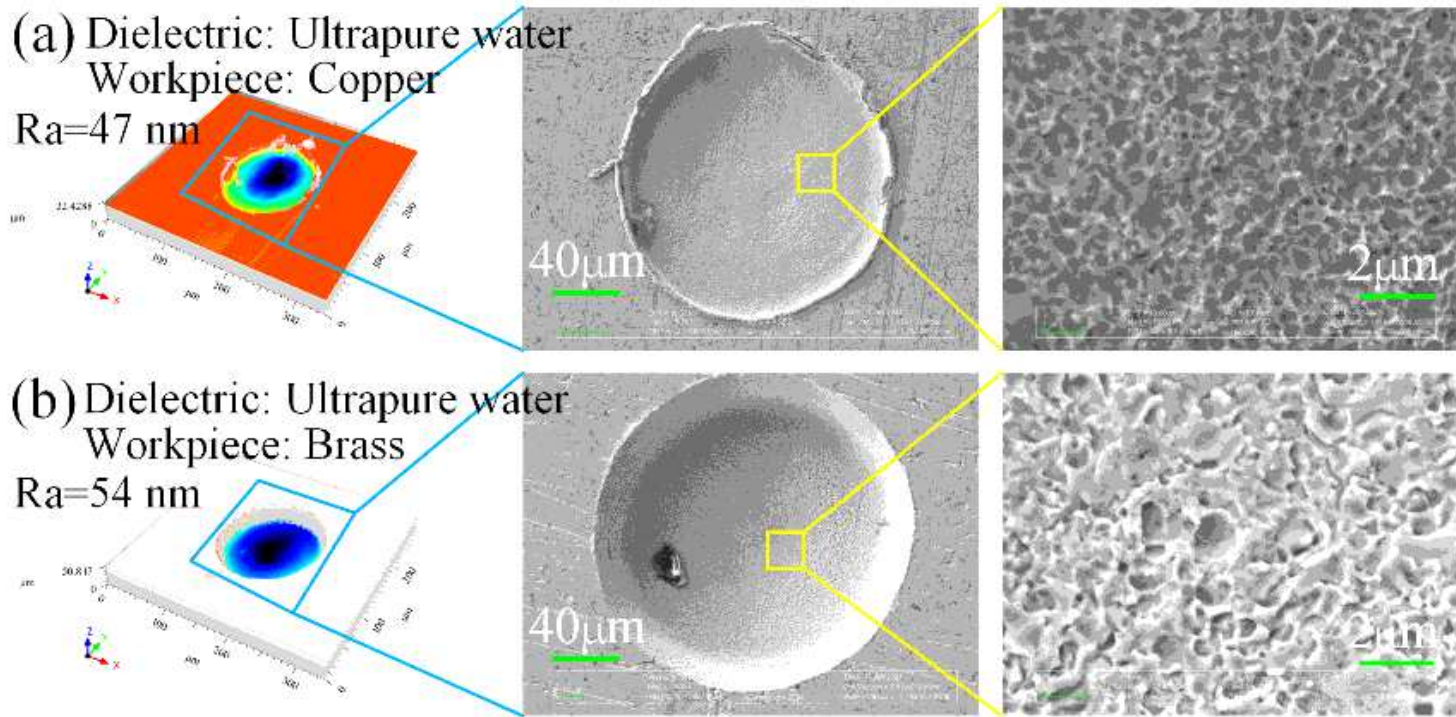


Figure 20

WLI and SEM images of different workpieces machined in ultrapure water: (a) copper and (b) brass.

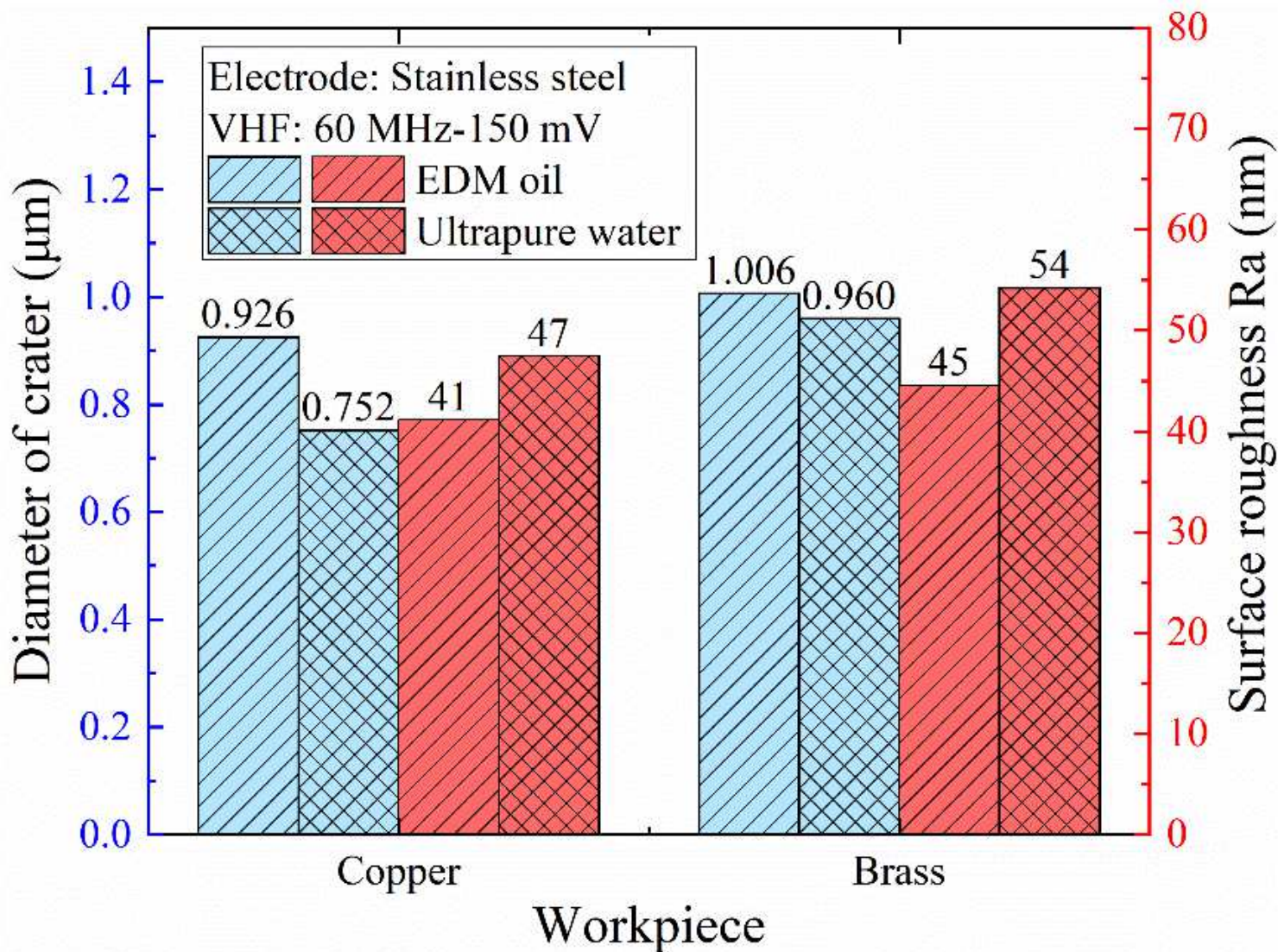


Figure 21

Diameter of crater and Ra with different workpiece materials and dielectric fluids.